Tribology International 103 (2016) 647–667

Contents lists available at ScienceDirect

Tribology International

journal homepage: www.elsevier.com/locate/triboint

# On the influence of conformity on wheel–rail rolling contact mechanics

Julio Blanco-Lorenzo, Javier Santamaria *, Ernesto G. Vadillo, Nekane Correa

*Department of Mechanical Engineering, University of the Basque Country UPV/EHU, Alda. Urquijo s/n, Bilbao, 48013 Spain*

ARTICLE INFO

*Article history:*
Received 20 May 2016
Received in revised form
19 July 2016
Accepted 24 July 2016
Available online 28 July 2016

*Keywords:*
Wheel–rail contact
Conformal contact
Rolling contact
FE modelling

ABSTRACT

The aim of this work is to assess the effects of conformity on local contact related quantities at the wheel–rail interface such as traction distributions, subsurface stresses and frictional work distributions. For this purpose conformal contact analyses are carried out by means of Finite Element (FE) models, and also with the exact rolling contact theory approach developed by Kalker, which has been appropriately adapted by the authors in order to take into account some of the effects of conformity. On the other hand, equivalent cases are analysed without taking into account the effects of conformity. In this way, the validity of the hypothesis of non-conformity is evaluated in different cases with varying degrees of conformity.

© 2016 The Authors. Published by Elsevier Ltd. This is an open access article under the CC BY-NC-ND license (http://creativecommons.org/licenses/by-nc-nd/4.0/).

## 1. Introduction

An important research activity has been carried out in the last years on vehicle-track interaction, including TrioTRAIN Project [27]. One of the most crucial aspects in this field is the wheel–rail contact modelling [2,34]. This modelling is specially important for the dynamic analysis of both a train negotiating a sharp curve as well as a train passing through a turnout [18,24]. Most wheel–rail rolling contact theories used in rail vehicle related studies have been developed on the basis of some simplifying assumptions which enable a considerable simplification of the wheel–rail contact problem. One of the commonly made assumptions is that the contact is punctual (i.e. the dimensions of the contact patch are much smaller than the characteristic dimensions of the contacting bodies), which implies flatness of the contact area and assimilation of the local behaviour of the contacting bodies to that of the elastic half-space. In the case of wheel–rail conformal contact there is a curved contact patch in the lateral direction, so that this assumption does not hold.

In many cases the hypothesis of non-conformal wheel–rail contact is reasonable, but there are situations such as the contact of wheel flange root with rail gauge corner during inscription in tight curves, in which conformal contact takes place. Moreover, in these situations usually severe contact conditions are encountered, with high tractions and slip velocities, and accurate determination of these are necessary in order to properly assess the wear and fatigue damage in the wheel–rail interface.

In the literature several references concerning conformal contact can be found, starting with the pioneer works of [36] and [30], for example in [15,46,29,10,14]. Most of the previous works focus on the normal part of the contact problem, and the tangential part is not incorporated in the analysis. Three important contributions in which both the normal and tangential parts of the contact problem are treated are those of [26] and the more recent of [39] and [9].

In this work the effects of conformity on the normal and tangential parts of wheel–rail rolling contact are investigated, extending the work presented in [8]. The study is mainly based on analyses with detailed FE models of the wheel–rail interface. Complementing these, analyses are carried out following the exact rolling contact theory approach developed by Kalker, both taking into account some of the effects of conformity, or completely disregarding any of such effects, as was originally developed. In this way the influence of conformity and the adequacy of the assumption of non-conformity can be assessed in different situations with varying degrees of conformity.

## 2. Description of the analysis methods

### 2.1. Non-conformal exact rolling contact theory

Kalker's exact rolling contact theory [21,22] is considered the most precise wheel–rail rolling contact theory. It has been widely employed in numerous wheel–rail contact mechanics related studies, e.g. [5,6,12,17,20,48]. It is applicable to general non-Hertzian contact geometries, and to transient as well as to steady state rolling contact problems. It is a boundary element method which resolves the local elastic field of the contacting bodies in an exact way (in the sense that "exact" has in a numerical method),

* Corresponding author.
*E-mail address:* javier.santamaria@ehu.eus (J. Santamaria).

http://dx.doi.org/10.1016/j.triboint.2016.07.017
0301-679X/© 2016 The Authors. Published by Elsevier Ltd. This is an open access article under the CC BY-NC-ND license (http://creativecommons.org/licenses/by-nc-nd/4.0/).

**Nomenclature**

| | |
|---|---|
| $a$, $b$ | longitudinal and lateral semi-axes of a contact patch obtained via a non-conformal analysis, or longitudinal and lateral half-sides or sides of each rectangular element of the discretization of the potential contact area (m) |
| $A$, $B$ | coefficients of the quadratic function approximating the normal undeformed distance between two contacting bodies ($m^{-1}$) |
| $B_{ij}$ | influence coefficient; displacement or displacement difference in direction $i$ due to unit load in direction $j$ (m/Pa) |
| $Cx$ | longitudinal curvature of the wheel ($m^{-1}$) |
| $C_{xi}$, $C_{yi}$ | principal curvatures of each body $i$ in contact ($m^{-1}$) |
| $d$ | maximum distance between the contours of the contact patches obtained with a conformal and with a non-conformal analysis for the same case (m) |
| $F_1$-$F_5$ | auxiliary functions defined in Appendix A for the calculation of the influence coefficients of rectangular elements with bilinear traction distribution in the elastic half-space ($m^2$ for $F_1$ and $m^3$ for the rest) |
| $G$ | modulus of rigidity (Pa) |
| $J_1$-$J_6$ | integral expressions for the calculation of the influence coefficients of the elastic half-space, defined in Appendix A (m) |
| $K$ | dimensionless elastic constant depending on the elastic properties of the two contacting bodies |
| $L$ | dimension of each rectangular element of the discretization of the potential contact area, either longitudinal ($a$) or lateral ($b$) (m) |
| $l_x$, $l_y$, $l_z$ | cosine directors of the direction of the axis of rotation of the wheel in the global coordinate system: $l_x = -\sin(\psi) \times \cos(\Phi)$; $l_y = \cos(\psi) \times \cos(\Phi)$; $l_z = \sin(\Phi)$ |
| $P_{nl}$, $P_{sl}$ | components of an applied load $P$ at a point $J$ in the principal directions $n$ and $s$ of another point $I$ (N) |
| $P_{fric}$ | frictional power density at each point in the contact patch, equal to the local slip velocity times the local tangential traction ($W/m^2$) |
| $R$, $r_i$ | rolling radius of a point of the wheel profile or in the contact area (m) |
| $r_{ij}$ | auxiliary variables defined in Appendix A for the calculation of the influence coefficients of rectangular elements with bilinear traction distribution in the elastic half-space (m) |
| $r_{nom}$ | nominal rolling radius of the wheel (m) |
| $T$ | surface traction, normal or tangential (Pa) |
| $u_y$, $u_z$ | lateral and vertical displacements of the wheelset with respect to the centre of the track, in global reference system (m) |
| $V$ | travelling speed of the wheelset (m/s) |
| $W_{fric}$ | integrated frictional work in the rail after one wheel passage ($J/m^2$) |
| $w_{long}$, $w_{lat}$ | rigid slip velocities or shifts in longitudinal and lateral directions of a point in the contact area (m/s or m) |
| $x$, $s$ | longitudinal coordinate and lateral curvilinear coordinate in the local contact reference system (m) |
| $x_i$, $y_i$ | longitudinal and lateral coordinates of a point in a planar contact area with respect to the reference point (m) |
| $x_{ledg}$, $x_{tredg}$ | longitudinal coordinates of leading and trailing edge of the contact patch at a given lateral position of it (m) |
| $y_L$, $z_L$ | Cartesian coordinates of the lateral profiles of the wheel and the rail, in their local reference system (m) |
| $y_{sc,i}$, $z_{sc,i}$ | horizontal and vertical coordinates of the intersection of the rolling circle described by a point in the surface of the wheel with a vertical plane perpendicular to the longitudinal direction, in global reference system (m) |
| $y_{w,i}$ | lateral coordinate of a point of the wheel profile, in the local reference system of the wheelset (m) |
| $\alpha$, $\alpha_i$ | angular difference in the lateral direction (rad) |
| $\beta$ | angle defining the orientation of the principal directions of the Hertzian undeformed distance function between two bodies, with respect to the principal planes of curvature of one of the bodies at the contact point (rad) |
| $\gamma$ | angle between the principal planes of curvature of two contacting bodies with Hertzian geometry at the contact point (rad) |
| $\delta$, $\delta_i$ | local contact angle or slope at each point of the lateral profile of the potential contact area (rad) |
| $\Delta Ap$ | variation of the approach between the two contacting bodies in the current time step, in a transient rolling or shift case (m) |
| $\Delta x$ | longitudinal dimension of each rectangular element of the mesh of the potential contact area (m) |
| $\Delta x_i$ | longitudinal distance between a plane perpendicular to the longitudinal direction and the centre of the rolling circle corresponding to a point of the wheel profile (m) |
| $\theta_i$ | angle between the local $y_w$-$z_w$ plane of the wheel and the radial plane passing through each point in the potential contact area (rad) |
| $\nu$ | coefficient of Poisson |
| $\xi$, $\eta$ | longitudinal and lateral creepages |
| $\varphi$: | spin creepage ($m^{-1}$) |
| $\Phi$, $\psi$ | roll and yaw angles of wheelset (rad) |
| $\Omega$ | angular velocity of the wheel (rad/s) |

making use of predefined influence coefficients and the principle of superposition around the contact zone. The division of the elements of the contact area into exterior (i.e. non-contacting), adhesion, and slip elements is performed iteratively, via an active set strategy.

The theory was implemented first in the computer programme DUVOROL and later in CONTACT [38]. In recent years several extensions to the programme have been developed, see for example [41,50], including the capability to treat conformal contact, the consideration of a third body layer in the wheel–rail interface, the introduction of variable friction coefficients depending on the local slip velocities, and the use of FFTs in order to speed up the discrete convolution operations arising in the resolution of the contact problem.

In its original form, the theory is applicable to linear elastic or viscoelastic bodies, which are also homogeneous and isotropic, in the framework of small displacements, in the absence of inertial forces (i.e. it is an elastostatic contact theory), in conditions of dry contact, and to punctual or non-conformal contact situations, where the contact patch dimensions are much smaller than the typical dimensions of the contacting bodies.

Assuming homogeneous and isotropic elastic bodies and non-

conformal contact implies that the local behaviour of the contacting bodies can be assimilated to that of the elastic half-space, which is known in advance. Assuming non-conformal contact also implies flatness of the contact area. The limitation to homogeneous and isotropic bodies can be overcome if the appropriate influence coefficients are used, as it is done for example in [45] for the case of elastic layered bodies. In a similar way, the limitation pertaining to non-conformity can be overcome using the particular influence coefficients for the specific geometry of the contacting bodies, as explained in [26] and [39]. However, in all these cases the analytic expressions of the influence coefficients in the space domain are not available, as they are for the homogeneous elastic half-space. The assumption of a flat contact area is relevant for the calculation of the normal undeformed distances and the rigid slip velocities or creepages at each point in the potential contact area, which are fundamental input variables for the normal and tangential parts of the contact problem respectively. The limitation related to the flatness of the contact area can be overcome if the normal undeformed distances and the creepages are calculated taking into account the correct contact geometry, with varying contact angles and rolling radii at each point, as is explained later.

Regarding the limitation of the absence of inertial forces, in [44] it has been verified that these have a negligible influence on wheel–rail contact mechanics at usual travelling speeds, which are considerably lower than the wave speeds in steel.

Apart from the exact wheel–rail rolling contact theory implemented in CONTACT, other more simplified models can be found which are able to treat conformal contact, as those presented in Chapter 8.5 of [19] and in [31], or STRIPES, see [4,33].

In this work, cases of conformal contact are analysed with CONTACT, deliberately discarding the effects related to conformity, in order to investigate the effects resulting from conformity, comparing the results obtained with and without taking into account these effects.

### 2.2. Finite element models

The Finite Element Method offers a very flexible framework to treat general non-linear problems, making possible to analyse complex geometries and to include if necessary the effects of non-linear geometry and material properties, inertial effects and frictional contact interactions. The solutions obtained with the FE models in the different cases analysed are considered as the reference in this work. The main disadvantage of these models is the high computational cost, on the one hand because of the high nonlinearity of the models due to the contact interaction, and on the other hand because the volume and not just the surface of the contacting bodies needs to be meshed, and providing a fine mesh around the contact if detailed results are sought in this zone. As a consequence the sizes of these models easily reach orders of magnitude of hundreds of thousands of degrees of freedom or more.

In this work static finite element models are used, built with the commercial software ABAQUS/Standard [1]. A portion of both contacting bodies near the contact zone is meshed with linear 8-node brick elements, and a fine mesh is provided in the contact zone, with a resolution of around 20 elements in each semi axis of the contact patch. Some details of the mesh of one of the models built are shown in Fig. 1.

A surface to surface frictional contact pair is defined between both contacting bodies, and the contact constraints are enforced with the penalty method, with properly adjusted penalty stiffness values. In this way, regularisation of the “hard” interfacial constitutive behaviour laws (see e.g. Chapter 36 of [1]) is achieved -specifically, a piecewise polynomial regularisation as described in Section 5.2.3 of [47]. Regarding the interfacial tangential behaviour, Coulomb's friction law with a constant coefficient of friction is used, in the FE models as well as in the other types of models used in this work (i.e. non-conformal exact rolling contact theory, and its extension to conformal contact). The material for the contacting bodies considered here and in the rest of the models shown in this paper is steel, with linear elastic and isotropic behaviour, a Young's modulus of 210 GPa and a coefficient of Poisson of 0.30. The steady rolling state is reached applying prescribed displacements and rotations to the wheel in consecutive steps, in a non-linear static simulation.

In other recent wheel–rail contact related studies with finite element models, e.g. [11,7,51,37,49], the entire wheel and a larger section of the rail are modelled, and details of the vehicle and of the track structure are included. In contrast, as mentioned above, in this work only a portion of both contacting bodies is meshed, though sufficient to ensure that the boundaries of the model do not affect the local stress field in the contact. Therefore the more general structural behaviour of the contacting bodies is not included in the study, because the focus in this work is on the local contact related quantities.

Another difference with the mentioned works is that those employ explicit dynamic transient models, while the models in this work are static. With the former models inertial forces in the rolling contact process are taken into account, and the explicit integration is effective in dealing with the severe nonlinearities associated with the contact conditions. The use of static models in this work is justified because here it is not intended to study any dynamic phenomena, and as mentioned in the previous section the local behaviour of the contacting bodies can be assumed to be

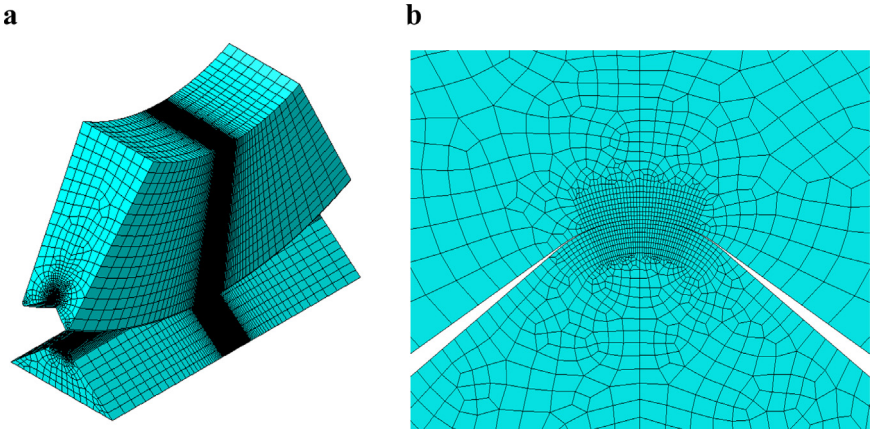


**Fig. 1.** Mesh of FE model for conformal contact study. (a) General view and (b) zoomed view in the contact area.

**Table 1**
Parameters of the non-conformal rolling contact test cases considered for validation of the FE models.

| Parameter | Value | Units |
|---|---|---|
| Lateral radius of curvature of wheel | ∞ | mm |
| Longitudinal radius of curvature of wheel | 500 | mm |
| Lateral radius of curvature of rail | 300 | mm |
| Coefficient of friction | 0.30 | – |
| Normal load | 80 | kN |
| Contact angle | 0 | º |
| Young's modulus of wheel and rail material | 210 | GPa |
| Coefficient of Poisson of wheel and rail material | 0.30 | – |

unaffected by inertial effects at conventional rolling speeds. In this way, some drawbacks associated with transient dynamic models are avoided (e.g. the transient vibrations at the beginning of the simulation, and the need to model longer sections in the rolling direction and to simulate the rolling through a longer distance until these are faded out), and quite detailed results are achieved in the contact zone without incurring in too high computational costs. Another recent example in which a quasistatic 3D FE model is used to conduct a detailed wheel–rail contact mechanics study can be found in [32].

### 2.2.1. *Validation of the FE models*

In this section some comparisons are made between the results obtained with FEM on the one hand, and those obtained with CONTACT on the other hand, for some non-conformal wheel–rail rolling contact test cases, in order to validate the FEM analysis methodology used in this work.

The main input data of the test cases shown here are listed in Table 1.

In Fig. 2 the creepage-creep force curves obtained with CONTACT and with FEM are compared, for varying longitudinal and lateral creepages. In Fig. 2a, the longitudinal creepage is variable and the lateral creepage is zero, and in Fig. 2b, the longitudinal creepage is zero and the lateral creepage is variable. As can be seen in the figure, the curves obtained with FEM provide slightly lower creep forces than those obtained with CONTACT for the same creepages, but the differences are quite small: for the different creepage conditions tested, the maximum difference seen in the resulting contact force is around 2.5% with respect to the traction bound.

Figs. 3 and 4 show the distribution throughout the contact patch of the tangential tractions and relative slip velocities (i.e. the slip velocities divided by the travelling speed) respectively, computed both with CONTACT and with FEM for the case with zero

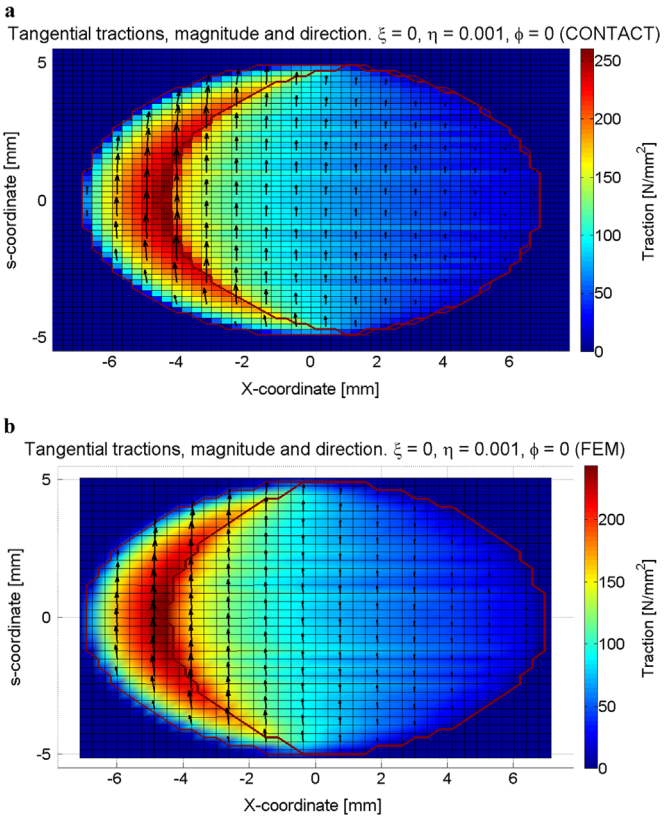


**Fig. 3.** Tangential traction distribution in non-conformal rolling contact with zero longitudinal creepage and lateral creepage of 0.1%. (a) Results computed with CONTACT and (b) results computed with FEM.

longitudinal creepage and 0.1% lateral creepage. As can be seen in the figures, the correspondence of the results from the FE model with those from CONTACT is very good.

Lastly, in Table 2 some of the main results for the same case shown in Figs. 3 and 4, obtained with the Hertzian theory, with CONTACT and with FEM, are compared. The differences between the results obtained with the different analysis methods are small, even in the maximum surface stresses and slip velocities, which are local quantities. The maximum differences are seen in the magnitudes related to the tangential part of the contact problem; specifically the maximum difference in the results shown in the table occurs in the integrated frictional work distribution after a wheel passage, and is around 7.5%. As can be seen in the table, the magnitudes related to the tangential part of the contact problem

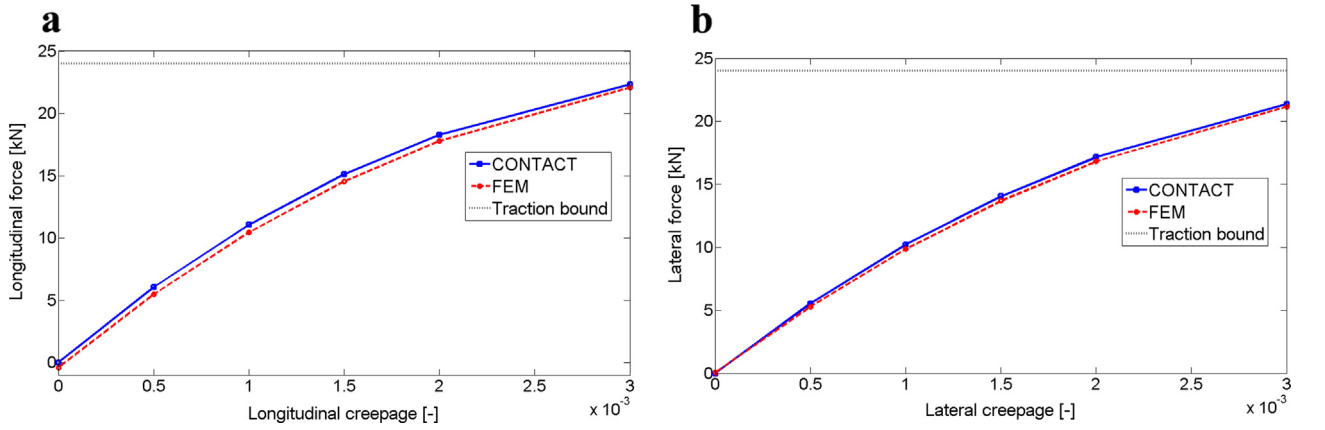


**Fig. 2.** Creepage-creep force curves for non-conformal rolling contact obtained with FEM and with CONTACT. (a) Zero lateral creepage and varying longitudinal creepage, (b) zero longitudinal creepage and varying lateral creepage.

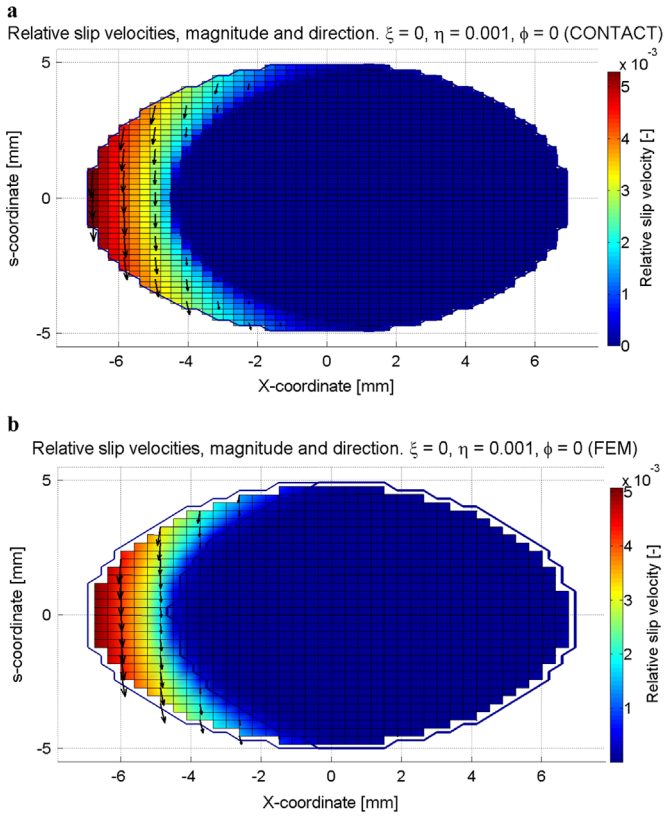


**Fig. 4.** Relative slip velocity distribution in non-conformal rolling contact with zero longitudinal creepage and lateral creepage of 0.1%. (a) Results computed with CONTACT and (b) results computed with FEM.

**Table 2**
Comparison of main results for non-conformal rolling contact test case with zero longitudinal creepage and lateral creepage of 0.1%, obtained with Hertzian theory, CONTACT and FEM.

| Result | Hertz | CONTACT | FEM |
|---|---|---|---|
| Longitudinal contact patch semi-axis (mm) | 6.946 | 6.9 | 6.937 |
| Lateral contact patch semi-axis (mm) | 4.935 | 4.9 | 4.95 |
| Normal approach between contacting bodies (mm) | 0.08825 | 0.08839 | 0.08874 |
| Maximum normal pressure (MPa) | 1114 | 1120 | 1121 |
| Maximum tangential traction (MPa) | | 259.9 | 243.0 |
| Maximum relative slip velocity (-) | | $5.279 \times 10^{-3}$ | $5.064 \times 10^{-3}$ |
| Maximum frictional work density (mJ/mm$^2$) | | 1.445 | 1.336 |

computed with FEM are slightly lower than those computed with CONTACT. This is attributed to the use of the penalty formulation in the FE model in order to enforce the contact constraints, which introduces some flexibility in the contact interface which is not present in the CONTACT model. Regarding the contact patch dimensions, it has to be noted that the accuracy of the reported results from CONTACT and FEM are limited by the element size used in the contact patch, which is $0.30 \times 0.20$ mm in the CONTACT analyses, and $0.375 \times 0.30$ mm in the case of the FEM analyses (longitudinal $\times$ lateral dimension). Nevertheless, the contact patch shapes obtained with the different analysis types are nearly coincident when plotted one over the other.

In conclusion, the comparison of the results obtained with the FE models with the results from CONTACT and the Hertzian theory in the different non-conformal contact test cases is favourable, and therefore the FE models are validated for the type of contact mechanics analyses performed in this work.

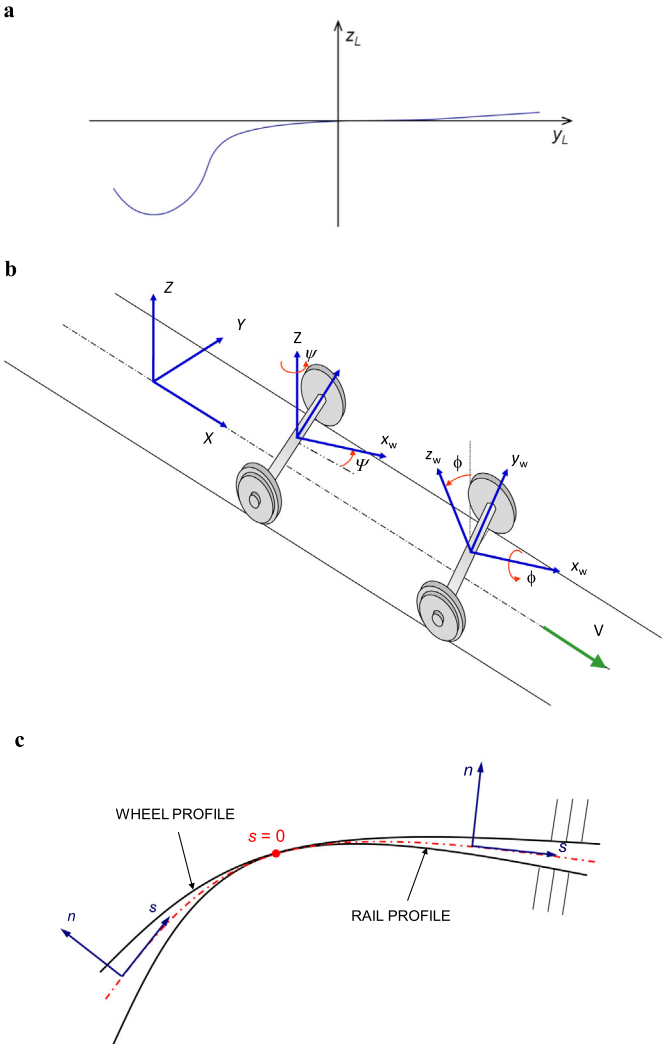


**Fig. 5.** Coordinate systems used for the study of wheel–rail conformal contact. (a) Local coordinate systems of the wheel and rail profiles (a wheel profile is shown in the figure), (b) global Cartesian coordinate system and wheelset local Cartesian coordinate system and (c) local contact coordinate system, with $x$ axis (not shown) perpendicular to the plane of the figure.

### 2.3. *Exact rolling contact theory including the effects of conformity*

In order to study conformal contact cases with less computational cost than with FE models, Kalker's exact rolling contact theory has been programmed in MATLAB. In the following sections the effects of conformity that are taken into account in the programmed version of the exact rolling contact theory are explained, and are contrasted with what is done in the non-conformal exact theory.

First, the different coordinate systems which are used are introduced and depicted in Fig. 5.

- Local coordinate systems of the wheel and rail profiles: 2D Cartesian coordinate systems with axes $y_L$ (lateral) and $z_L$ (vertical), with the origin in the nominal rigid contact points of the respective profiles.
- Global Cartesian coordinate system, with axes $X$, $Y$, $Z$: its origin is located in the centre of the track, at the height of the origin of the coordinate system of the rail profile. The global $X$ axis is oriented in the longitudinal (rolling) direction, the $Y$ axis is

oriented in the lateral direction, pointing towards the left wheel and the $Z$ axis completes the right handed Cartesian coordinate system, pointing upwards. The $X$ and $Y$ axes are contained in the (usually horizontal) plane of the track.

- Wheelset local Cartesian coordinate system, with axes $x_w$, $y_w$, $z_w$: its origin is located at the central point of the wheelset axis of revolution. It is oriented according to the wheelset yaw ($\psi$) and roll ($\Phi$) angles as follows: 1) rotation of $\psi$ angle around global $Z$ axis and 2) rotation of $\Phi$ angle around local $x_w$ axis.
- Local contact coordinate system: Cartesian coordinate system defined according to the tangential plane at each point of the contact area, with its three principal orthogonal directions designated as the longitudinal (rolling) direction $x$, the lateral direction $s$, and the normal direction $n$. The local vectorial quantities in the contact such as surface displacements and tractions, as well as the influence coefficients, are expressed in this coordinate system.

Regarding the solution algorithms, on the one hand the normal part of the contact problem is solved with an algorithm similar to Kalker's NORM [21,22], with the difference that the checks for the elements in the contact and exterior areas are performed simultaneously at each iteration (i.e. in the same iteration, multiple elements may be changed from the contact to the exterior area and vice versa). On the other hand, the tangential part of the contact problem is solved with an algorithm similar to Kalker's TANG [21,22], also with the difference that the checks for the elements in the adhesion and slip areas are performed simultaneously at each iteration. Additionally, for the tangential part of the contact problem Vollebregt's ConvexGS algorithm [40] has also been tried.

The rolling contact problems were tried to be solved first directly as steady state rolling contact problems. When convergence was not achieved in the tangential part of the contact problem with neither of the algorithms used, the problems were solved as a sequence of transient rolling contact cases until the steady state was reached. The TANG algorithm was not effective in all the transient cases either, but with ConvexGS a solution was achieved for the tangential part of the contact problem in all the transient cases that were tried.

### 2.3.1. Influence coefficients for conformal geometries

As explained in [26] and [39], the local behaviour of conformal bodies around the contact is different from that of the elastic half-space. In those works this issue is tackled by computing numerically with linear FE models the necessary influence coefficients for the geometries analysed. This approach has the drawback of the need to compute the influence coefficients for each particular case, and also the difficulty of separating the total elastic displacements provided by the FE analyses into global deflections and local displacements around the contact, the latter being the wanted ones for use in the contact model.

It has long been recognised that the use of the half-space Boussinesq influence function for the normal part of the contact problem is a good approximation for moderate levels of conformity (with total contact angle variations less than about 45º), see for example [29,10,14,26,3]. It can be verified that this is also true for the other direct influence coefficients, i.e. the ones that relate the displacements in a given direction to a load in the same direction. In contrast, in some of the crossed influence coefficients, i.e. the ones that provide the displacements in a given direction due to a load in a different direction, greater differences are seen between those of the half-space and those of conformal bodies. The most pronounced differences are seen in the case of the influence coefficients $B_{sn}$, i.e. the ones which provide the displacements in the lateral tangential direction due to normal pressures (and vice versa, in the influence coefficients $B_{ns}$). However, if the loads are rotated according to the local principal directions of each point where the displacements are observed, as shown in Fig. 6, it is seen that the half-space influence coefficients can still provide a reasonably good approximation of the influence coefficients for conformal geometries.

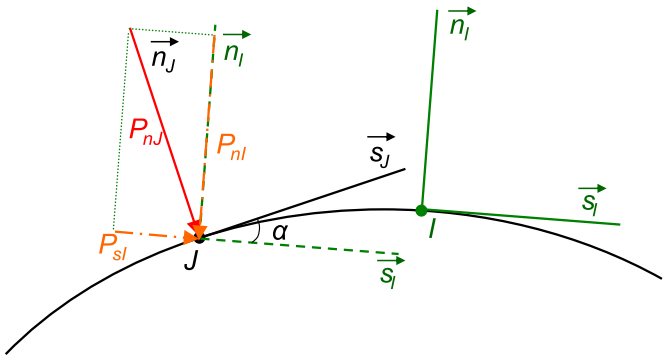


**Fig. 6.** Illustration of the combination of the influence coefficients of the half-space in order to approximate the influence coefficients for conformal geometries. Influence coefficient $B_{iIjJ}$: displacement of point $I$ along direction $i$, due to a unit load in direction $j$ at point $J$.

As shown in the figure, the load applied at a given point $J$ is decomposed in the $s$ and $n$ directions of point $I$ where the displacements are observed, according to Eq. (1) below:

$$\vec{P}_{nJ} = \vec{P}_{nI} + \vec{P}_{sI} = \left|\vec{P}_{nJ}\right| \cdot \cos(\alpha) \cdot \vec{n}_I + \left|\vec{P}_{nJ}\right| \cdot \sin(\alpha) \cdot \vec{s}_I \tag{1}$$

Following the reasoning depicted in Fig. 6, the influence coefficients for conformal geometries are approximated with the influence coefficients of the half-space, according to Eqs. (2–10):

$$B_{xx\_conf} \approx B_{xx} \tag{2}$$

$$B_{xs\_conf} \approx B_{xs} \times \cos(\alpha) + B_{xn} \times \sin(\alpha) \tag{3}$$

$$B_{sx\_conf} \approx B_{sx} = B_{xs} \tag{4}$$

$$B_{ss\_conf} \approx B_{ss} \times \cos(\alpha) + B_{sn} \times \sin(\alpha) \tag{5}$$

$$\begin{aligned} B_{nn\_conf} &\approx B_{nn} \times \cos(\alpha) - B_{ns} \times \sin(\alpha) \\ &= B_{nn} \times \cos(\alpha) + B_{sn} \times \sin(\alpha) \end{aligned} \tag{6}$$

$$B_{xn\_conf} \approx B_{xn} \times \cos(\alpha) - B_{xs} \times \sin(\alpha) \tag{7}$$

$$B_{sn\_conf} \approx B_{sn} \times \cos(\alpha) - B_{ss} \times \sin(\alpha) \tag{8}$$

$$B_{nx\_conf} \approx B_{nx} = -B_{xn} \tag{9}$$

$$\begin{aligned} B_{ns\_conf} &\approx B_{ns} \times \cos(\alpha) + B_{nn} \times \sin(\alpha) \\ &= -B_{sn} \times \cos(\alpha) + B_{nn} \times \sin(\alpha) \end{aligned} \tag{10}$$

In Eqs. (2–10), $\alpha$ is the angle between the principal directions $s$/$n$ of the point where the load is applied and those of the point where the displacement is calculated as shown in Fig. 6 (in this work only lateral angular differences are considered; the geometry in the longitudinal direction is considered non conformal). On the other hand $B_{ij}$ are the influence coefficients representing the displacement in direction $i$ due to a load in direction $j$; the ones with no further suffix are those of the elastic half-space, the expressions of which are given in Appendix A, and the ones with suffix "*conf*" are those estimated for conformal geometries. In the case of the non-conformal analyses, the angle $\alpha$ is assumed to be always zero and the used influence coefficients are, evidently, those of the elastic half-space.

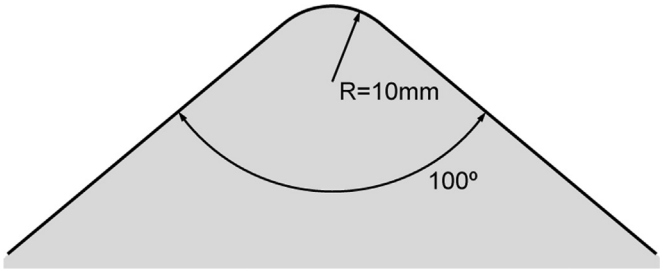


**Fig. 7.** Convex body considered for the calculation of the influence coefficients shown in Fig. 8. The body is prismatic in the longitudinal $x$ direction.

**Table 3**
Parameters for the calculation of the influence coefficients for a convex conformal geometry.

| Parameter | Value | Units |
|---|---|---|
| Longitudinal half side of the loaded rectangle | 0.12 | mm |
| Lateral half side of the loaded rectangle | 0.105 | mm |
| Radius of circular part of lateral profile of the convex body | 10 | mm |
| Total wedge angle of the convex body | 100 | º |

In order to assess the adequacy of the above equations, next the influence coefficients $B_{sn}$ of the half-space are compared with those calculated numerically via FEM for a prismatic convex body, and with those estimated for the same convex body using the above Eq. (8). The convex body considered has a constant cross section in any plane perpendicular to the longitudinal $x$ axis. This cross section is composed of a circular arc and two straight lines which form a total angle of 100º as shown in Fig. 7, and has a plane of symmetry in the middle of the circular arc. The load applied is a constant pressure over a rectangle on the surface aligned with the principal directions $x$ and $s$ and centred in the lateral plane of symmetry of the convex body (at lateral coordinate $s=0$). Other relevant parameters considered in this calculation are listed in Table 3.

The resulting influence coefficients of the surface displacements are shown in Fig. 8, along the lateral direction, in a cross section at a distance equal to the longitudinal dimension of the loaded rectangle from the centre of the loaded rectangle. As can be seen in Fig. 8, there is a high discrepancy between the influence coefficients $B_{sn}$ of the half-space and those calculated numerically for the convex body of Fig. 7. On the other hand, combining the influence coefficients of the half-space according to Eq. (8) gives a good approximation of the influence coefficients $B_{sn}$ of the convex

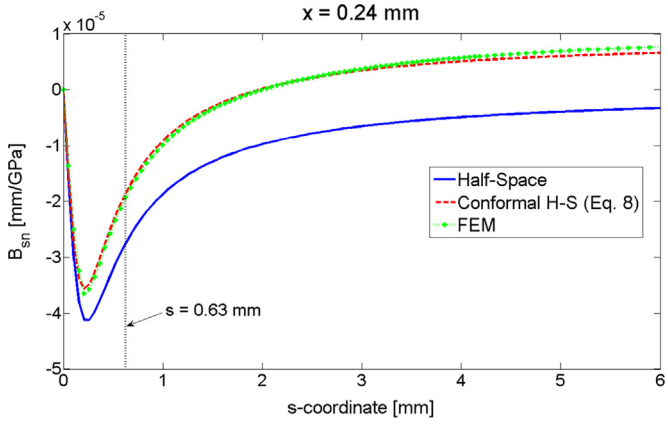


**Fig. 8.** Comparison of influence coefficients $B_{sn}$ for the half-space and for the convex body of Fig. 7. Blue solid line: half-space. Red dashed line: estimation for convex body according to Eq. (8). Green dotted line with + marks: calculated with FEM for convex body. (For interpretation of the references to color in this figure legend, the reader is referred to the web version of this article.)

body calculated numerically with FEM.

Looking at Eq. (8) and Fig. 6 it can be seen that for convex bodies, the component $P_{sI}$ of the applied normal pressure $P_{nJ}$, which arises due to conformity in the lateral direction, tends to produce tangential displacements in the surrounding points $I$ in the opposite sense to those produced by the component $P_{nI}$, which draws the surrounding points towards where the load is applied. This can be verified looking at the influence coefficients $B_{sn}$ calculated in Fig. 8 for the convex body of Fig. 7, where it is seen that they have a lower absolute magnitude than those of the half-space, and at some distance away from the point of application of the load they even reverse direction. On the other hand, for concave bodies the effect will be the contrary, i.e. both components $P_{nI}$ and $P_{sI}$ of the applied load will produce tangential displacements in the same sense in the surrounding points. The net effect in the contact between a convex body and a concave body is that the contact normal pressures cause tangential displacement differences, as stated in [39], even in the case of contacting bodies with similar elastic properties. As a result the elastic quasiidentity property cannot be applied in the case of frictional conformal contact, and there will be a certain degree of coupling between the normal and the tangential parts of the contact problem. In order to solve the coupled contact problem with the programmed exact rolling contact theory, the Panagiotopoulos process [22] is employed, i.e. the normal and tangential problems are solved sequentially, keeping the tangential tractions fixed at each iteration for the normal problem, and conversely, keeping the normal tractions fixed at each iteration for the tangential problem, until convergence is achieved.

It is remarkable how fast the influence coefficients $B_{sn}$ for conformal geometries deviate from those of the half-space. For example, in Fig. 8 it can be seen that at lateral $s$ coordinate 0.63 mm, the difference between the influence coefficient $B_{sn}$ of the half-space and that of the convex body calculated with FEM is already around 20% of the peak influence coefficient $B_{sn}$ shown in the figure. At this position the angular difference with respect to the centre of the loaded rectangle is only 3.6º. This rapid deviation is well explained with the last term of Eq. (8), due to the fact that the influence coefficients $B_{ss}$ are of higher magnitude than the influence coefficients $B_{sn}$, and also because of the rapid change of the $\sin(\alpha)$ term around $\alpha$ values of 0.

A further aspect to note is that the influence coefficients $B_{sn}$ are an order of magnitude lower than the direct influence coefficients, so that it may be thought that they have a low influence on the contact problem. However, it is seen that they can have a high influence on the tangential part of the contact problem, in contrast to what was assumed in [26]. In order to illustrate this, a case of conformal contact has been calculated with the programmed exact contact theory with and without performing the correction for conformity in the $B_{sn}$ influence coefficients according to Eq. (8), and also with FEM. The considered case is the static contact of a concave roller symmetric in the lateral direction and with a transverse radius of 10.5 mm pressed against a convex rail with the same geometry shown in Fig. 7. The described geometry of the contacting bodies is the same as that of the model shown in Fig. 1. This is one of the cases that was considered in [8]. Other parameters of the calculation are listed in Table 4.

In Fig. 9 the obtained lateral tangential tractions along the lateral direction in the middle cross section of the contact patch (because of symmetry in the longitudinal direction, the longitudinal tangential tractions are zero at this cross section) are plotted, with the three models considered.

On the one hand, it is seen that there is an appreciable difference between the results obtained with the exact contact theory with and without performing the correction for conformity in the $B_{sn}$ influence coefficients. The notable influence of the $B_{sn}$ influence coefficients on

**Table 4**
Parameters for the calculation of the static compression case with similar materials and lateral conformity shown in Fig. 9.

| Parameter | Value | Units |
|---|---|---|
| Radius of circular part of lateral profile of the concave roller | 10.5 | mm |
| Longitudinal radius of curvature of roller | 653.7 | mm |
| Coefficient of friction | 0.30 | – |
| Normal load | 80 | kN |
| Mean contact angle | 0 | º |
| Yaw angle | 0 | º |

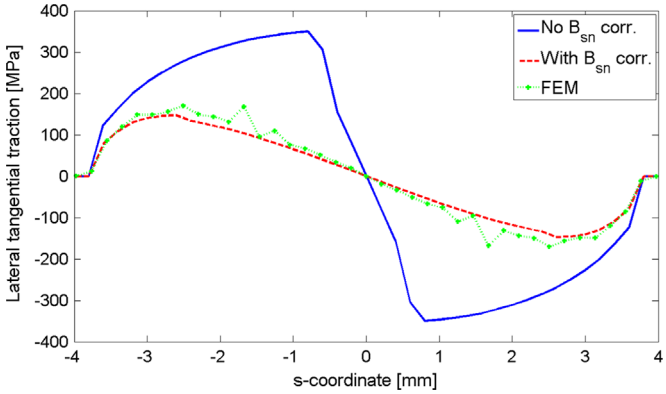


**Fig. 9.** Comparison of lateral distributions of tangential tractions obtained in conformal compression of elastically similar bodies, at the middle cross section of the contact patch. Blue solid line: programmed exact contact theory without correction for conformity in the $B_{sn}$ coefficients. Red dashed line: programmed exact contact theory with correction for conformity in the $B_{sn}$ coefficients. Green dotted line with + marks: FEM solution. (For interpretation of the references to colour in this figure legend, the reader is referred to the web version of this article.)

the results of the tangential part of the contact problem, despite their lower magnitude with respect to the $B_{ss}$ coefficients, can be attributed to the fact that the normal pressures are much higher than the tangential tractions in the considered case: the maximum values of normal pressure and tangential traction obtained with the FE model are around 1200 and 170 MPa respectively.

When the correction for conformity is performed, the tangential displacement differences caused by the normal pressures partially counteract the tangential shifts imposed at each point in the contact patch, which are equal to the approach or normal shift times the sine of the angle between the direction of the imposed normal shift and the local normal at each point. As a result, the resulting tangential tractions are considerably lower than without the conformity correction applied, and the whole contact patch remains in adhesion. On the contrary, in the case of not performing the conformity correction the tangential tractions reach the saturation limit and there is sliding in most of the contact patch.

On the other hand, it is seen that the tangential traction distribution obtained with the programmed exact contact theory, performing the correction for conformity in the influence coefficients, approaches that of the FEM, although with apparently somewhat lower tangential tractions obtained with the former. It could be argued that the obtained precision with the programmed exact contact theory is worse than should be expected from an exact contact theory. Nevertheless, it is difficult to make conclusive statements here, due to the level of noise present in the solutions obtained with both the programmed exact contact theory and the FE model (in the solutions obtained with the programmed exact contact theory the noise occurs mainly in the longitudinal direction, and is hardly noted in the lateral cross section presented in Fig. 9).

Lastly, Fig. 10 shows the lateral distributions of normal tractions

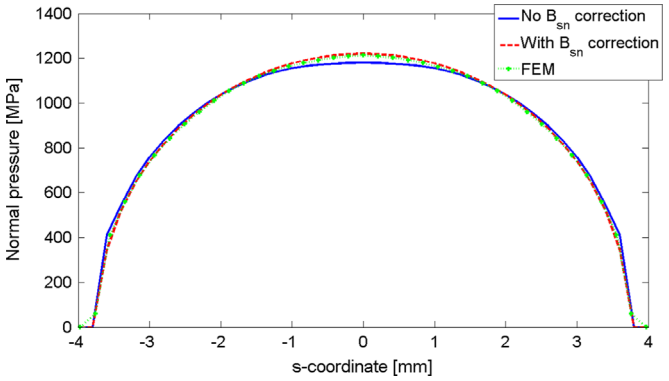


**Fig. 10.** Comparison of lateral distributions of normal tractions obtained in conformal compression of elastically similar bodies, at the middle cross section of the contact patch. Blue solid line: programmed exact contact theory without correction for conformity in the $B_{sn}$ coefficients. Red dashed line: programmed exact contact theory with correction for conformity in the $B_{sn}$ coefficients. Green dotted line with + marks: FEM solution. (For interpretation of the references to colour in this figure legend, the reader is referred to the web version of this article.)

obtained with the same models as those considered in Fig. 9, at the same location. As shown in the figure, the normal pressure distribution obtained with the exact contact theory performing the correction for conformity in the $B_{sn}$ influence coefficients, approaches well that obtained with the FE model. On the other hand, the pressure distribution obtained with the exact contact theory without performing the correction for conformity in the $B_{sn}$ influence coefficients is slightly different, with a maximum normal pressure that is about 3% lower than the maximum pressures obtained with the other two models. This happens as a result of the coupling between the normal and the tangential parts of the contact problem with conformal geometries, as will be further discussed in Section 3.2.

### 2.3.2. *Normal undeformed distances*

The normal undeformed distances throughout the potential contact area are the fundamental geometric input variables for the normal part of the contact problem. In this section the process followed for the calculation of the normal undeformed distances with conformal geometry is described. The wheel is considered a perfect body of revolution, and the rail straight in the rolling direction. The contact is assumed to be conformal only in the lateral direction, so the contact patch can be curved only in this direction, and will be considered flat in the longitudinal direction. Both contacting bodies are considered smooth, without roughness, but the process could be easily extended to include roughness.

The main input data are as follows:

a) Lateral profiles of both contacting bodies. Without loss of generality these are assumed to be given by a list of value pairs representing the Cartesian coordinates ($y_L$, $z_L$) of the set of points chosen to represent the profiles. The points have to be given in consecutive order, but neither of their coordinates need be monotonically increasing or decreasing; there may be vertical sections for example.
b) Nominal rolling radius of the wheel.
c) Position and orientation of the wheel with respect to the rail. This will be generally given by a lateral displacement $u_y$, a vertical displacement $u_z$, a yaw angle $\psi$ and a roll angle $\Phi$. Besides, the option to include a rail cant angle is also included.
d) Parameters for the discretization of the potential contact area: the potential contact area is discretized with equal rectangular elements and will normally be centred around the rigid point of contact. The necessary parameters are the upper and lower bounds in the longitudinal and in the lateral direction, and the

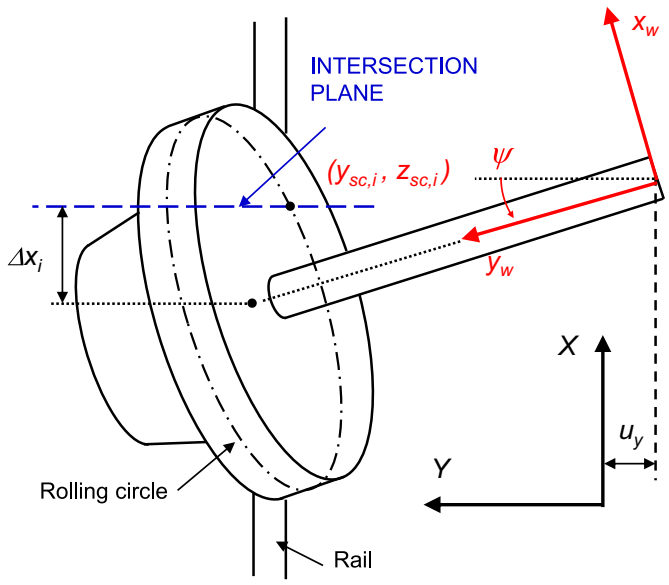


**Fig. 11.** Intersection point ($y_{sc,i}$, $z_{sc,i}$) of the rolling circle of one of the points of the wheel profile with a plane perpendicular to the longitudinal direction. Plan view.

number of elements in each direction.

The main steps followed for the calculation of the normal undeformed distances are listed below. Each of the steps 1 to 6 is performed for each longitudinal position in the discretization of the potential contact area.

1) Calculation of the longitudinal distance $\Delta x_i$ between the current longitudinal position in the discretization of the potential contact area and the points in the revolution axis of the wheel corresponding to each of the points representing the lateral profile of the wheel.
2) Calculation of the intersection curve between the wheel and the plane perpendicular to the longitudinal direction located at the current longitudinal position. Fig. 11 shows schematically the intersection of the rolling circle of one of the points of the wheel profile with a plane perpendicular to the longitudinal direction, with some of the relevant parameters in the calculation. In order to calculate the intersection between the rotated wheel and a plane perpendicular to the longitudinal direction, a development similar to that shown in Appendix D of [26], for the calculation of the locus of the possible rigid contact points in the wheel, is followed. For a given point of the lateral cross section of the wheel profile, the Cartesian coordinates of the intersection point of its corresponding rolling circle with the plane are given as:

$$y_{sc,i} = u_y + y_{w,i} \times l_y - \frac{1}{l_y}\left(\Delta x_i \times l_x - l_z\left(\frac{\Delta x_i \times l_x \times l_z + l_y\sqrt{(1-{l_x}^2){r_i}^2 - {\Delta x_i}^2}}{{l_y}^2 + {l_z}^2}\right)\right) \quad (11)$$

$$z_{sc,i} = r_{nom} + u_z + y_{w,i} \times l_z - \frac{\Delta x_i \times l_x \times l_z + l_y\sqrt{(1-{l_x}^2){r_i}^2 - {\Delta x_i}^2}}{{l_y}^2 + {l_z}^2} \quad (12)$$

where:

$y_{sc,i}$, $z_{sc,i}$: horizontal and vertical coordinates of the intersection point (in global reference system).
$y_{w,i}$: lateral coordinate of the considered point of the wheel profile (in the local reference system of the wheelset).
$r_i$: rolling radius of the considered point of the wheel profile.
$\Delta x_i$: longitudinal distance between the intersection plane and the centre of the rolling circle of the considered point.

3) Parameterisation of the calculated intersection curve of the wheel with the lateral curvilinear coordinate $s$, representing its length.
4) Search for the location of the origin of the $s$ coordinate on the intersection curve of the wheel, which is defined to be on the point at the minimum distance from the chosen reference or central point of the potential contact area, projected to the current longitudinal position.
5) Calculation of the discretized profile of the wheel, interpolating on the intersection curve of the wheel at the lateral positions of the discretization of the potential contact area.

Steps 3 to 5 above are performed in a similar way for the rail, although they are performed only once and not at each longitudinal position, since the lateral profile of the rail is the same at all longitudinal positions.

6) Calculation of the normal undeformed distance between both contacting bodies at each lateral position of the discretization, as the projection over the local normal direction of the vector between the points on the rail and on the wheel having the same $s$ coordinate, as shown in Fig. 12. In this way, contact is assumed to occur between points with the same $s$ (and also $x$) coordinates. This assumption is justified in the framework of small displacements, where the undeformed distances and elastic displacements are much lower than the typical dimensions across the contact patch.

For the calculation of the local normal direction at each lateral position of the discretization, the reference lateral profile of the potential contact area is taken into account. This reference lateral profile is calculated as an interpolation between the lateral profile of the rail and the reference lateral profile of the wheel, weighted with the stiffness of each of the contacting bodies. The reference lateral profile of the wheel is taken as the intersection between the wheel and the plane perpendicular to the longitudinal direction located at the reference or central longitudinal position of the potential contact area.

It is worth mentioning that, as the normal contact problem is quite sensitive to small variations in the input normal undeformed distances, the interpolations performed in step 5) of the above described process for the calculation of the normal undeformed distances may have an influence on the obtained normal pressure distributions. For Hertzian geometries, linear interpolation is seen to be sufficient, but for non-Hertzian geometries, like in the case

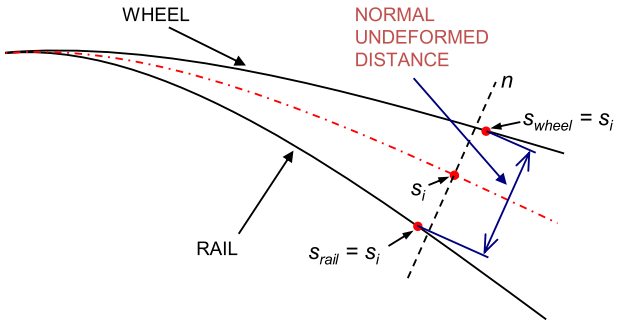


**Fig. 12.** Calculation of normal undeformed distance in conformal contact. The normal undeformed distances are calculated between points with the same $x$ and $s$ coordinates in both contacting bodies.

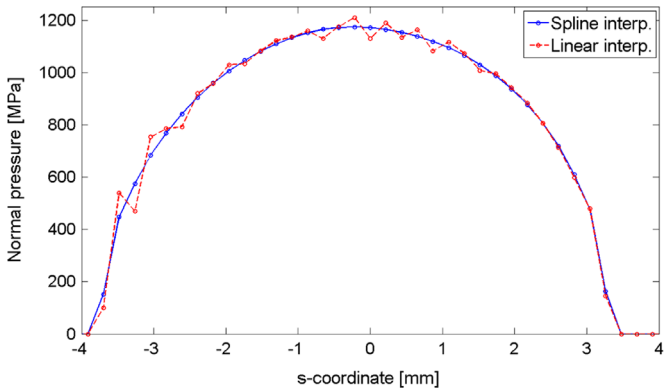


**Fig. 13.** Comparison of lateral distributions of normal pressure close to the central longitudinal position in the contact patch, in a case with conformal contact. Blue solid line: spline interpolation for the calculation of the normal undeformed distances. Red dashed line: linear interpolation. (For interpretation of the references to colour in this figure legend, the reader is referred to the web version of this article.)

shown in Fig. 15a in Section 3.1 (which would be considered Hertzian if not taking into account the conformity), it has been observed that using linear interpolations noisy pressure distributions result, unless a considerably finer discretization is used for the input profiles of wheel and rail than for the potential contact area where the contact problem is solved. With spline interpolations, the mentioned noise in the pressure distributions is eliminated. In order to illustrate this, in Fig. 13 the obtained lateral distributions of normal pressure with different interpolation types for the calculation of the normal undeformed distances are compared, for the mentioned case of conformal contact. In the shown case, the contact patch is discretized with approximately 36 elements in the lateral direction, and the wheel and rail profiles are defined with approximately 85 and 150 points respectively in the same zone. The results shown in this work have been obtained using spline interpolations for the calculation of the normal undeformed distances.

Lastly, in the case of the non-conformal analyses, instead of following the above described process for the calculation of the normal undeformed distances, a semi-Hertzian representation of them is used, according to the following considerations:

- A constant longitudinal curvature for the wheel is considered, corresponding to that of the central or reference point in the contact area.
- Realistic (non-Hertzian) lateral undeformed profile representation.
- The yaw angle of the wheel is not taken into account.

### 2.3.3. Creepages

The creepages or imposed rigid shifts at each point of the potential contact area are the fundamental kinematic input variables for the tangential part of the contact problem. In the non-conformal analyses the imposed rigid shifts at each point are defined in terms of the longitudinal, lateral and spin creepages according to Eqs. (13) and (14) below:

$$w_{long} = -\left(\xi + \varphi \times y_i\right) \times V \tag{13}$$

$$w_{lat} = -\left(\eta - \varphi \times x_i\right) \times V \tag{14}$$

On the other hand, with non-planar contact areas, as explained in [31], the notion of creepages as applicable to the whole contact area loses its sense, and it becomes necessary to compute the local rigid shifts or slip velocities at each point. Despite this, in some cases presented in Section 3, creepage values are reported. These creepage values correspond to the central or reference points of the contact patch in each case.

The local rigid slip velocities at each point are computed as the projections of the velocity vector of the considered point of the wheel on the local principal tangential directions, as a function of the linear and angular velocities of the wheel, the distance of the point from the axis of revolution of the wheel, and the orientations of the axis of revolution of the wheel and the local tangent plane at the considered point. The rigid velocities of the rail are assumed to be zero. The resulting expressions for the longitudinal and lateral rigid slip velocities are given below.

$$w_{long} = V + \Omega \times r_i \times \left(-\cos(\theta_i) \times \cos(\psi) - \sin(\theta_i) \times \sin(\psi) \times \sin(\Phi)\right) \tag{15}$$

$$w_{lat} = \Omega \times r_i \times \left(-\cos(\delta_i) \times \cos(\theta_i) \times \sin(\psi) + \cos(\delta_i) \times \sin(\theta_i) \times \cos(\psi) \times \sin(\Phi) - \sin(\delta_i) \times \sin(\theta_i) \times \cos(\Phi)\right) \tag{16}$$

In the above formulas, the linear velocity $V$ of the wheel is assumed perfectly aligned with the rolling direction and therefore not contributing to the lateral creepage. In the general case, the contributions of the linear velocity of the wheel to the longitudinal and lateral creepages can be expressed in terms of its components in the global Cartesian coordinate system $V_x$, $V_y$ and $V_z$, as $V_x$, and $[-V_y \times \cos(\delta_i) + V_z \times \sin(\delta_i)]$, respectively.

The angles $\theta_i$ and $\delta_i$, which are in general variable at each point in the potential contact area, are depicted in Fig. 14.

In Eqs. (15) and (16), the angular velocity vector of the wheel is assumed to be aligned with its symmetry or revolution axis. If this were not the case, the only necessary change would be to replace the angles $\psi$ and $\Phi$ in said equations by the appropriate angles describing the orientation of the angular velocity vector of the wheel.

On the other hand, in the case of transient analyses (normal and tangential shifts, and transient rolling), the tangential shifts produced by the variation in the approach between the two contacting bodies is taken into account as the projection of the variation of the approach on the local lateral $s$ direction at each point, as was mentioned previously in Section 2.3.1, according to Eq. (17) below:

$$w_{lat} = -\Delta Ap \times \sin(\alpha_i) \tag{17}$$

where $w_{lat}$ is the rigid shift in the lateral (s) direction, and $\alpha_i$ is the angle (contained in a vertical plane perpendicular to the longitudinal direction) between the direction of $\Delta Ap$ and the local normal at each point, see Fig. 14.

## 3. Results and discussion

First, the different cases studied are described. Situations of steady rolling and of static contacts are analysed. Simple geometries with varying degrees of conformity are considered, with constant principal curvatures in the contact region. The rail has zero longitudinal curvature and a transversal convex radius of curvature of 10 mm in all cases. The wheel or roller has different transversal concave curvatures, as listed in Table 5. In the same table, the main characteristics of the resulting contact patches are shown.

Another geometrical parameter for the different cases considered is the mean contact angle, i.e. the contact angle at the central or reference point in the contact patch. This will be 0º or 45º, as indicated in the corresponding sections. The rest of the relevant parameters are as listed in Table 4, unless otherwise indicated.

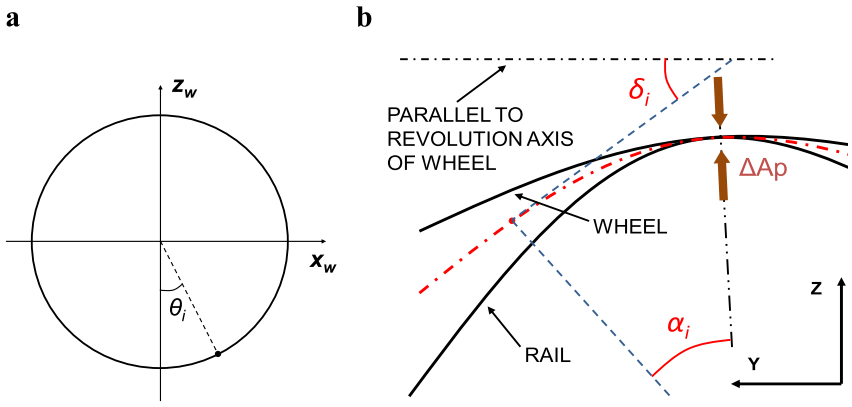


**Fig. 14.** Definition of angles $\theta_i$ (a), $\delta_i$ and $\alpha_i$ (b) for each point in the potential contact area.

**Table 5**
Geometrical parameters of the different conformal contact cases analysed.

| Case no. | Transverse radius of curvature of wheel (mm) | Total lat. contact angle variation (deg) | Longitudinal dimension of contact patch (mm) | Lateral dimension of contact patch (mm) |
|---|---|---|---|---|
| 1 | 10.5 | 43 | 16.6 | 7.2 |
| 2 | 11 | 29 | 18.4 | 5.2 |
| 3 | 12 | 22 | 19.2 | 4.0 |
| 4 | 15 | 14 | 20.6 | 2.7 |

**Table 6**
Contact patch areas and maximum normal pressures obtained in the different conformal contact cases analysed.

| Case no. | Contact patch area [mm$^2$] Conformal/Non-conformal | Maximum normal pressure [MPa] Conformal/Non-conformal |
|---|---|---|
| 1 | 102.9/97.28 | 1216/1203 |
| 2 | 78.65/76.47 | 1562/1551 |
| 3 | 60.60/59.70 | 2008/2002 |
| 4 | 44.69/44.30 | 2719/2716 |

### 3.1. Contact patch shapes

Fig. 15 shows the contact patch contours obtained considering different concave transversal curvature radii for the wheel as listed in Table 5, with a mean contact angle of 45º and a yaw angle of 3.54 mrad, corresponding to a lateral creepage of -0.5%. The figure also shows the limits between the adhesion and slip zones. In these cases most of the contact patches are in slip except for a central adhesion zone, due to the high mean contact angle and corresponding spin creepage. These contact patches have been computed with the exact contact theory with and without considering the effects of conformity, and in the case with the highest degree of conformity of Fig. 15a, also with FEM. The correspondence between the contact patches obtained in this case with the conformal exact contact theory and with the FEM is very good.

The areas of the contact patches and maximum normal pressures obtained in each case with the exact contact theory with and without considering the effects of conformity are listed in Table 6. The contact patch area and maximum normal pressure obtained in Case 1 with the FEM are 103.5 mm$^2$ and 1214 MPa respectively, very similar to the corresponding values obtained with the conformal exact contact theory.

As can be seen in Fig. 15, the shapes of the contact patches obtained with the non-conformal and with the conformal analyses begin to differ noticeably already with modest levels of conformity, as seen for example in Fig. 15c, in which the contact patch is spread over a lateral angle of around 22°. The obtained contact patches with the conformal analyses are not symmetric in the lateral nor in the longitudinal direction, due to the effects of the varying longitudinal curvature of the wheel in the lateral direction, and the yaw angle of the wheel.

Referring to the varying longitudinal curvature of the wheel ($Cx = \cos(\delta)/R$; $Cx$ being the longitudinal curvature of the wheel, $\delta$ the contact angle and $R$ the rolling radius at each point in the contact patch), which results mainly from the variation in the contact angle, its effect is more pronounced at higher contact angles. For example, considering a total contact angle variation in the contact patch of 40º, and the rest of the geometrical parameters as given above, with a mean contact angle of 0º the longitudinal curvature of the wheel varies only in about 6% in the contact patch with respect to its value at the central point, while its variation reaches nearly 70% with a mean contact angle of 45°. As a result, if the mean contact angle is changed to 0º in the cases shown in Fig. 15, the contact patches obtained with the conformal analyses are much more similar to those obtained with the non-conformal analyses, in which the longitudinal curvature of the wheel is considered constant and equal to that of the central point in the contact patch.

In order to assess the explained influence of the mean contact angle on the resulting differences between the contact patches obtained with the conformal and the non-conformal analyses, cases with the same contact geometry as that considered in Fig. 15a have been analysed for different values of the mean contact angle between 45° and 0°, maintaining the rest of the parameters. The results are summarised in Fig. 16 in terms of the difference between the shapes of the contact patch contours obtained with conformal and with non-conformal analyses. In order to quantify this difference between the conformal and non-conformal contact patches, the maximum distance between the contours of both contact patches is determined, and it is normalised with the length of the mean contact patch semi-axis. This normalised distance is designated as the difference ratio between conformal and non-conformal contact patches in Fig. 16. The mean contact patch semi-axis is taken as the square root of the product of the two principal semi-axes of the contact patch obtained with the non-conformal analysis in each case. Therefore the difference ratio between conformal and non-conformal contact patches is defined as distance $d$ divided by the square root of the product of $a$ and $b$; $a$, $b$ and $d$ being as indicated in Fig. 17, where two contact patches obtained with a conformal and with a non-conformal analysis are depicted.

With respect to the yaw angle of the wheel, it may be thought at first that its influence on the contact patch shape will be small, due to the small values which may realistically take in the wheel–

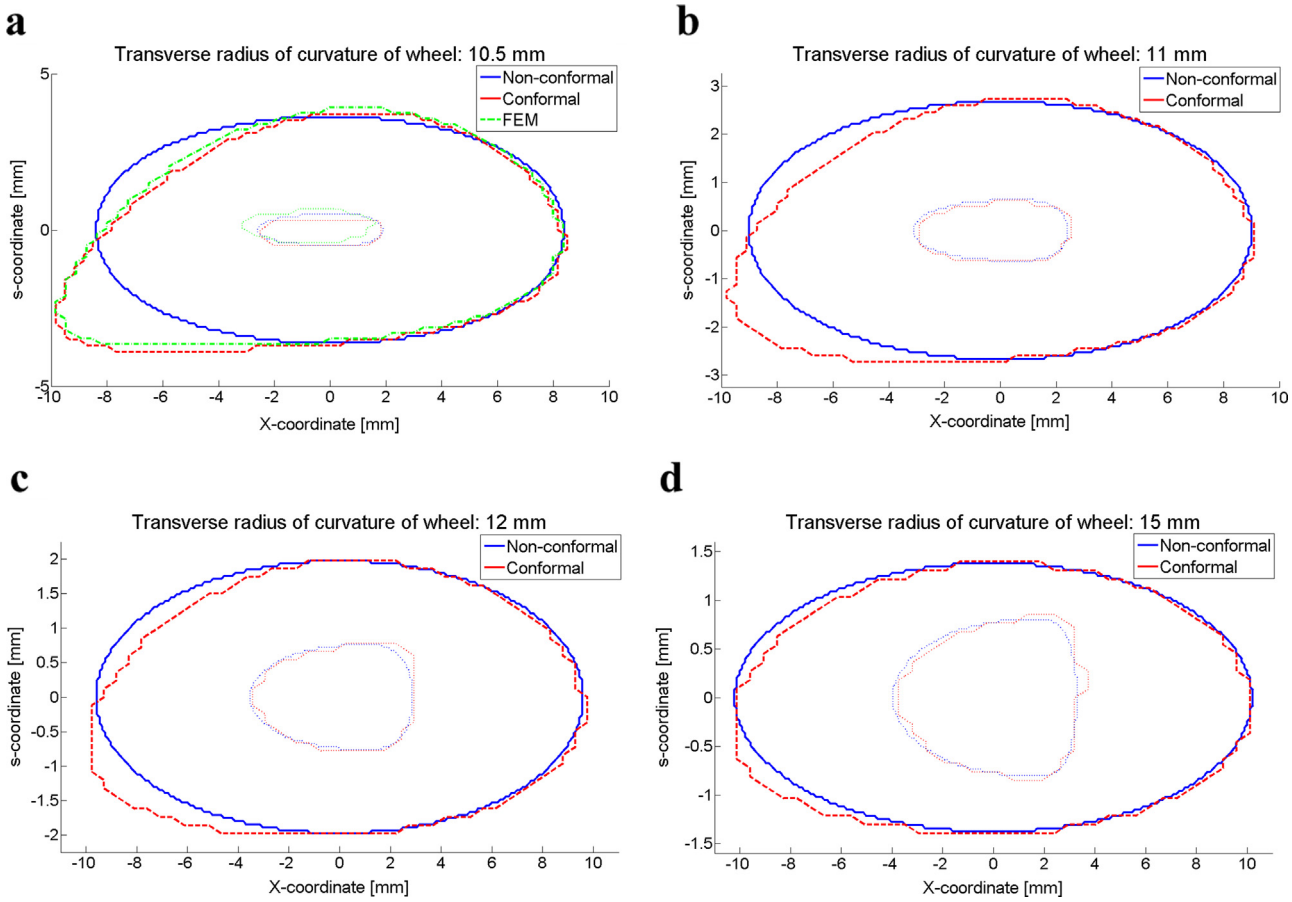


**Fig. 15.** Contact patch contours in conformal contact with a mean contact angle of 45º and a yaw angle of 3.54 mrad. Results computed with non-conformal exact contact theory marked as "Non-conformal" in solid blue lines, and those computed with conformal exact theory marked as "Conformal" in dashed red lines. Contact patch contours computed with FEM marked as "FEM" in dash-dotted green lines in (a). (For interpretation of the references to colour in this figure legend, the reader is referred to the web version of this article.)

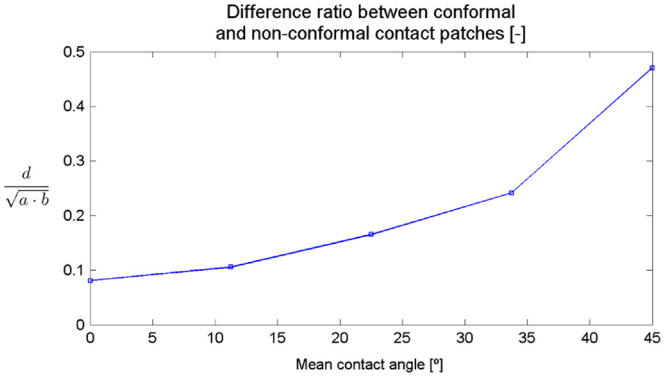


**Fig. 16.** Difference ratio between conformal and non-conformal contact patches as a function of the mean contact angle.

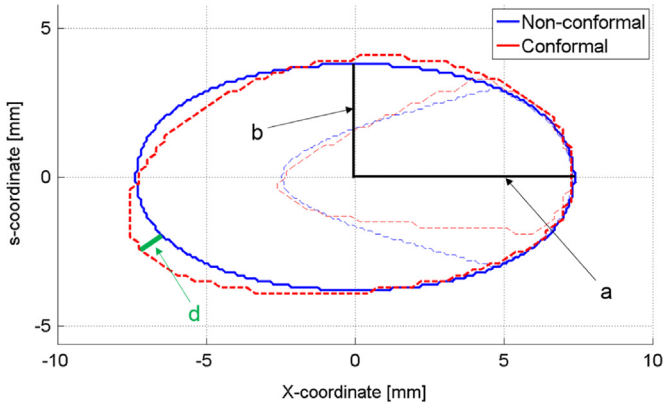


**Fig. 17.** Definition of the relevant dimensions $a$, $b$ and $d$ for the calculation of the difference ratio between conformal and non-conformal contact patches, in order to quantify the difference between the shapes of the different contact patches.

rail case (in the cases of Fig. 15, only 3.54 mrad, which is already a relatively severe yaw angle in wheel–rail rolling contact). This is so with non-conforming geometries, where it is usually assumed that the contact patches depend on the local geometries of the contacting bodies around the contact point but not on the (relatively small) angle between the planes containing their respective principal curvatures. From this it follows that with non-conforming geometries the contact patches can be assumed to be symmetric in the longitudinal direction regardless of the yaw angle of the wheel. However, with conforming geometries this is not applicable, as can be seen from the contact patch shapes shown in Fig. 15. This can be explained with a geometrical analysis of the combined undeformed distance function between the two contacting bodies. If quadratic undeformed surfaces are assumed for the two contacting bodies, the angle $\gamma$ between the principal planes of curvature of the two bodies in contact and the angle $\beta$ defining the orientation of the principal planes of the combined undeformed distance function as shown in Fig. 18 are related through Eqs. (18) and (19) below, see e.g. Appendix 2 of [19] (note that in the cited reference the nomenclature is different: the angles designated here as $\beta$ and $\gamma$, are designated as $\alpha$ and $\theta$ respectively in the cited reference):

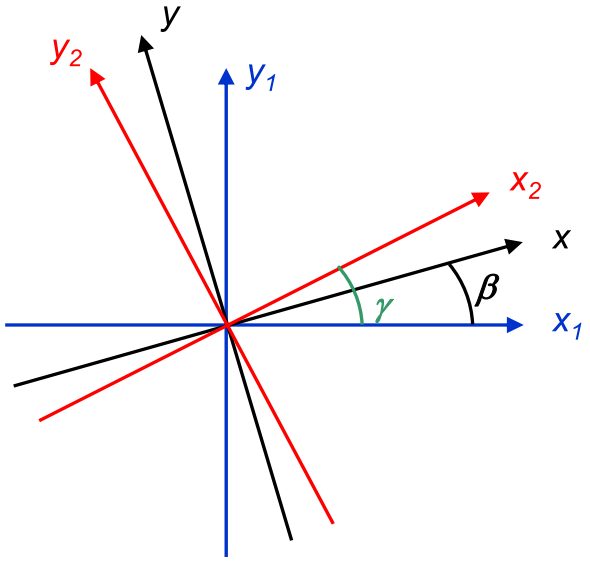


**Fig. 18.** Definition of orientation of principal planes of curvature of each of the two bodies in contact (with suffixes 1 and 2) and of the combined undeformed distance function (with no suffix).

$$|B-A| = \frac{1}{2}\left\{ (C_{x1}-C_{y1})^2 + (C_{x2}-C_{y2})^2 + 2(C_{x1}-C_{y1})(C_{x2}-C_{y2})\cos 2\gamma \right\}^{1/2} \quad (18)$$

$$\sin(2(\gamma-\beta)) = 1/2 \times |C_{x1}-C_{y1}|/(B-A) \times \sin(\pi-2\gamma) \quad (19)$$

where $C_{xi}$ and $C_{yi}$ are the principal curvatures of each body $i$ in contact, and $A$ and $B$ are the coefficients of the quadratic function approximating the undeformed distance between the two contacting bodies.

When all the principal curvatures are positive, i.e. convex, the angle $\beta$ will be in the same sense as the angle $\gamma$, and of lower value. However, when one of the curvatures is concave and closely conforming with the corresponding convex curvature of the other body, the angle $\beta$ can be much higher than the angle $\gamma$, and will be in the opposite sense. For example, substituting the principal curvatures of Case 1 shown in Fig. 15a in the above equations, the resulting angle $\beta$ is about 30 times higher than the angle $\gamma$. Therefore, with conforming geometries small yaw angles can cause appreciable orientation changes in the combined undeformed distance between the two contacting bodies, and hence in the resulting contact patch.

In cases such as those shown in Fig. 15, it is clear that the usual assumption in wheel–rail contact of quadratic undeformed distances in the rolling direction, even if using a realistic non-Hertzian transverse profile representation and varying longitudinal curvatures in the lateral direction, is inadequate for the accurate estimation of the contact patch shape, due to the high influence of the yaw angle with conformal geometries as described above. In this way, the need to properly calculate the normal undeformed distance at each point in the contact patch, as previously described, is justified. Nevertheless, it is worth noting that even in the case with the highest degree of conformity shown in Fig. 15a, the overall dimensions of the contact patch and the maximum contact pressure obtained with the non-conformal analysis, are very similar to those obtained with the conformal analyses, as can be seen in Table 6. The maximum contact pressures obtained with the different analyses are within a margin of about 1% in this case.

### 3.2. Coupling between normal and tangential problems

As has been mentioned before, one particular feature of frictional conformal contact is that there is a coupling between the normal and tangential parts of the contact problem, even when having contacting bodies with elastically similar properties as in the wheel–rail case. In order to evaluate the significance of this coupling, the same case of static conformal compression for which results are shown in Fig. 9, in which the total lateral contact angle variation in the contact patch is about 43°, has been computed without friction. The geometry is that of Case 1 of Table 5. The resulting lateral distributions of normal pressure in the middle cross section of the contact patch with and without friction are depicted in Fig. 19, computed with FEM.

The values of the maximum normal pressures obtained in this case with and without friction are of 1213 and 1244 MPa respectively; that is, the maximum pressure obtained in the frictionless case is about 2.5% higher than in the equivalent case with friction. The decrease in the normal pressure values in the frictional case with respect to the frictionless is not uniform across the width of the contact patch, but is maximum in the central position, at $s=0$ mm. This is because at this location the effects of the lateral tangential stresses at each side of the contact patch, which are symmetric about this point, sum up and is maximum: the tangential stresses at either sides of the contact patch tend to increase the normal undeformed distance in the central part.

Part of the decrease in the normal pressures in the frictional case is due to the fact that the tangential stresses that appear in the frictional case (see Fig. 9) sustain part of the resultant normal force in the contact. In this case, about 1.5 kN of the total normal load of 80 kN, i.e. about 1.85% of the normal load, is seen to be sustained by the lateral tangential stresses. This would explain a decrease of about 0.6% in the maximum value of the contact pressure, assuming Hertzian proportionality between the remaining part of the normal load sustained by the normal pressures and the maximum value of the contact pressure.

The computations performed with the conformal exact contact theory for the same case show a similar trend, although with a more reduced impact: the difference between the maximum normal pressures obtained with and without friction is just about 2%. In conclusion, some coupling between the normal and tangential parts of the contact problem is verified, although this is seen to be relatively limited. In other different rolling contact cases computed with the same contact geometry, with different values of spin and lateral creepage, a lower influence of the tangential stresses upon the normal pressures have been observed, even with higher levels of tangential traction.

Another way in which the coupling between the normal and tangential parts of the contact problem in conformal contact is

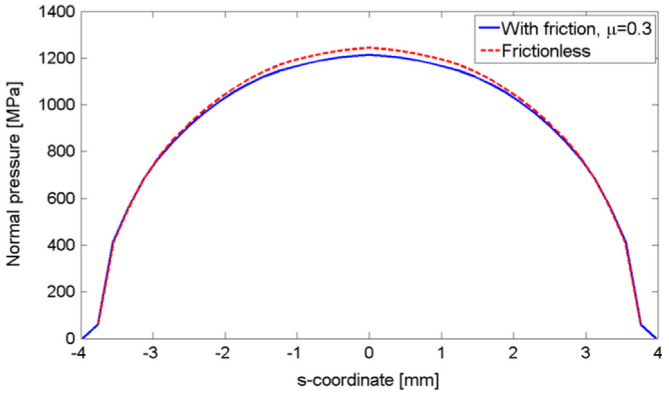


**Fig. 19.** Comparison of lateral distributions of normal pressures obtained in conformal compression of elastically similar bodies, at the middle lateral cross section of the contact patch. Blue solid line: frictional contact; coefficient of friction of 0.30. Red dashed line: frictionless contact. (For interpretation of the references to colour in this figure legend, the reader is referred to the web version of this article.)

manifested, is in the lateral shift of the position of the contact patch that occurs in cases where a net lateral force is transmitted in the contact. The lateral tangential stresses modify the normal undeformed distances in such a way that the contact patch tends to shift to the side towards which the concave body is pushing the convex one. In order to illustrate this effect, Fig. 20 shows schematically the lateral variation of the normal elastic displacements in the same convex body considered in Fig. 19, due to the "normal components" of the lateral tangential stresses acting on the surface of the body in the contact patch. The "normal components" of the lateral tangential stresses referenced here are analogous to the $P_{nI}$ force component shown in the contact force decomposition represented in Fig. 6.

Note that neither the elastic displacements caused by the remaining "tangential components" of the lateral tangential stresses, nor the elastic displacements caused by the normal pressures, are represented in this figure, because they are assumed to produce no shift in the lateral position of the contact patch. The "tangential components" of the lateral tangential stresses don't produce any normal displacement difference in the case of elastically similar contacting bodies due to the quasiidentity property, assuming that Eqs. (2–10) correctly represent the elastic behaviour of the contacting bodies around the contact area. And the normal pressures don't cause any lateral shift in the contact patch in this case due to the lateral symmetry of the contact geometry.

Fig. 20 also shows the lateral tangential stresses acting on the surface of the convex body, represented with arrows. These tend to be higher in the middle zone of the contact patch, due to the higher pressures and consequently higher values of the traction bound in this zone. As can be seen in the figure, the normal elastic displacements are positive or outwardly directed from the convex body in the left side of the contact patch, and negative or inwardly directed in the right side. In the concave body, considering that both the sign of the curvature of the contacting surface, and that of the lateral tangential stresses are opposite to those of the convex body, the corresponding elastic displacements will also be outwardly directed from the concave body in the left side of the contact patch, and inwardly directed in the right side. Therefore, the normal undeformed distance is seen to be reduced in the left side of the contact patch, and increased in the right side, and the lateral position of the contact patch will consequently be shifted to the left side (i.e. to the side towards which the concave body is pushing the convex one).

### 3.3. Lateral distribution of frictional work

In this section the lateral distributions of integrated frictional work in the rail after one wheel passage obtained with conformal and non-conformal analyses are compared. The frictional work in the rail after one wheel passage $W_{fric}$ at a given lateral position $s$ is obtained integrating the frictional power density $P_{fric}(x, s)$ along the longitudinal direction of the contact patch according to Eq. (20) below:

$$W_{fric}(s) = \frac{1}{V}\int_{x_{ledg}(s)}^{x_{tredg}(s)} P_{fric}(x, s)dx \tag{20}$$

Which, discretized in a mesh of equal rectangular elements with dimension $\Delta x$ in the longitudinal direction leads to the following expression:

$$W_{fric}(s_i) = \frac{\Delta x}{V}\sum_{x_i} P_{fric}(x_i, s_i) \tag{21}$$

Fig. 21 shows the lateral distributions of integrated frictional work in the rail after one wheel passage obtained considering the different concave transversal curvature radii for the wheel listed in Table 5, with an approximate mean contact angle of 45° and zero yaw angle. In the cases shown in this figure both the (nominal) longitudinal and lateral creepages are zero.

The frictional work distributions obtained with the conformal analyses are clearly biased towards the gauge side of the track, i.e. towards the side with increasing contact angles and decreasing $s$-coordinate values. This is because the longitudinal dimensions of the contact patches, as well as the magnitude of the slip velocities, are larger in this side. The larger dimensions of the contact patches at the zone with higher contact angles are the result of the lower longitudinal curvatures of the wheel, which vary across the contact patch as described previously in Section 3.1. The higher slip velocities in the same zone (in this case with a nominal longitudinal creepage of zero) are due to the more rapid variation of the rolling radii at higher contact angles. These higher slip velocities can give rise to more severe wear regimes, see for example [43,25,28], and the resulting lateral distributions of wear will be even more biased towards the gauge side than the frictional work distributions.

As the level of conformity decreases, the lateral distributions of frictional work obtained with the conformal analyses tend to converge to those obtained with the non-conformal analyses as expected, becoming more symmetric across the width of the contact. A further point to note is that the frictional work distributions obtained with the conformal exact theory reproduce the trends of the results obtained with the FE analyses, although the latter yield somewhat lower levels of frictional work.

Next, a case with a mean contact angle of 0° is considered. The geometry is that corresponding to Case 1 of Table 5, the yaw angle is 2 mrad, the longitudinal creepage is zero as before, and the lateral creepage is 0.2%. Fig. 22 shows the distribution throughout the contact patch of the tangential tractions and slip velocities computed with the FE model, and Fig. 23 the lateral distributions of frictional work computed for this case with the different analysis methods.

As can be seen in Fig. 22a, the tangential stress distributions and the adhesion and slip areas obtained with the FE model are not symmetrical around the longitudinal axis of the contact patch, in contrast to what is obtained with the non-conformal exact theory. This is due to the combination of the lateral creepage with the geometric spin, which is variable across the contact patch.

However, the integrated frictional work after a wheel passage is nearly symmetrical in the lateral direction, as can be seen in Fig. 23. This results from two opposing effects: first, the larger tangential stresses and slip area in the side towards which the wheel pushes the rail (i.e. towards decreasing $s$-coordinates), as is seen in Fig. 22a, and second, the larger slip velocities in the other side, as is shown in Fig. 22b. Both effects are due to the combined effect of the rigid slip velocities resulting from the applied lateral

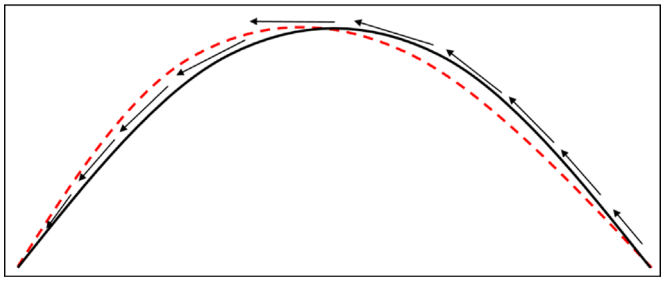

**Fig. 20.** Elastic displacements caused in convex body in conformal contact due to the normal components of the lateral tangential stresses. The undeformed profile is represented with solid black line, and the deformed profile with dashed red line. The lateral tangential stresses acting on the surface of the convex body are represented with arrows. (For interpretation of the references to colour in this figure legend, the reader is referred to the web version of this article.)

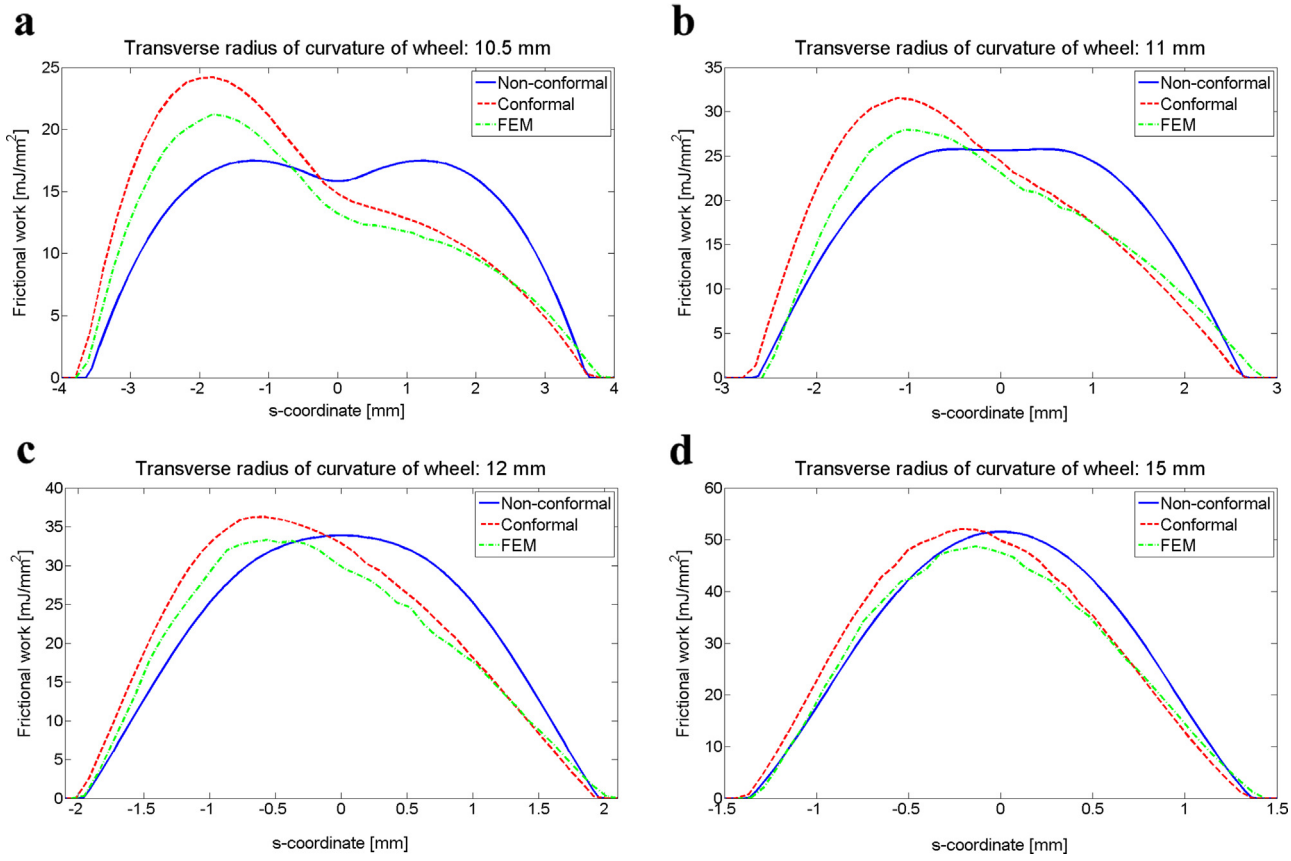


**Fig. 21.** Comparison of lateral distributions of integrated frictional work in the rail after one wheel passage in conformal contact with a mean contact angle of 45º and zero yaw angle. Results computed with non-conformal exact contact theory marked as "Non-conformal" in solid blue lines, results computed with conformal exact theory marked as "Conformal" in dashed red lines, and results computed with FEM marked as "FEM" in dash-dotted green lines. (For interpretation of the references to colour in this figure legend, the reader is referred to the web version of this article.)

creepage on the one hand, and those resulting from the geometric spin on the other hand. In the rear part of the contact patch (i.e. in the side with decreasing $X$-coordinates), where the slip area is located, in the side with increasing $s$-coordinates these have the same sense and therefore they sum up, and in the other side they have opposing senses.

Another aspect to note in Fig. 23 is the lateral shift effect of the contact patch resulting from the coupling between the normal and tangential parts of the contact problem, that was explained in Section 3.2. This can be appreciated comparing the blue (non-conformal analysis) and red (conformal analysis with exact contact theory) curves in the figure. The positions at which these curves fall to zero indicate the lateral limits of the calculated contact patches. Due to the lateral symmetry of the geometry of this case, the contact patch in the non-conformal analysis is centred in the lateral direction around the rigid point of contact located at the $s$-coordinate value of 0, but the contact patch in the conformal analysis is seen to be slightly shifted towards decreasing $s$-coordinates. Lastly, the integrated frictional work obtained with the FE model is somewhat lower than that obtained with the conformal exact theory, as before.

### 3.4. Subsurface stresses

In this section the same case of Section 3.2 is considered, i.e. a static conformal compression with a mean contact angle of 0º and the contact geometry of Case 1 of Table 5. Fig. 24 shows the contours of the von Mises equivalent stress in both contacting bodies in the lateral cross section at the central longitudinal position of the contact patch, calculated with FEM on the one hand, and calculated with half-space theory, taking into account the surface contact stresses obtained with the conformal exact contact theory on the other hand. In Fig. 25 the variations in the normal direction of the von Mises equivalent stresses computed with both methods at the central lateral position of the cross section shown in Fig. 24 are compared.

As can be seen from the FEM results in Figs. 24 and 25, the maximum value of von Mises equivalent stress takes place in the concave body, in this case the wheel. The values of maximum von Mises stress computed with the FE model in the wheel and in the rail are 794 MPa and 711 MPa respectively, i.e. the maximum von Mises stress in the wheel is about 12% higher than that in the rail. Part of this difference is caused by the superposition of the effect of the tangential stresses (with different sign in each of the contacting bodies) with that of the normal pressures, which happens to be more unfavourable in the case of the wheel: the values of maximum von Mises equivalent stress in the wheel and in the rail computed with the half-space theory are 759 MPa and 727 MPa respectively, i.e. about 4% higher in the wheel than in the rail.

According to the results obtained with the FE model, the points with maximum von Mises stress are located at about 2 mm from the surface in the wheel, and at 3 mm from the surface in the rail. Compared to the locations of the respective maxima obtained with the half-space calculation, which are approximately 2.5 mm and 2.25 mm from the surface respectively in wheel and rail, the point with maximum equivalent stress is moved towards the surface in the wheel, and to a greater depth below the surface in the rail.

Lastly, it has to be mentioned that the tangential tractions in the case considered here are relatively low. In cases with higher levels of tangential tractions, the points of maximum equivalent

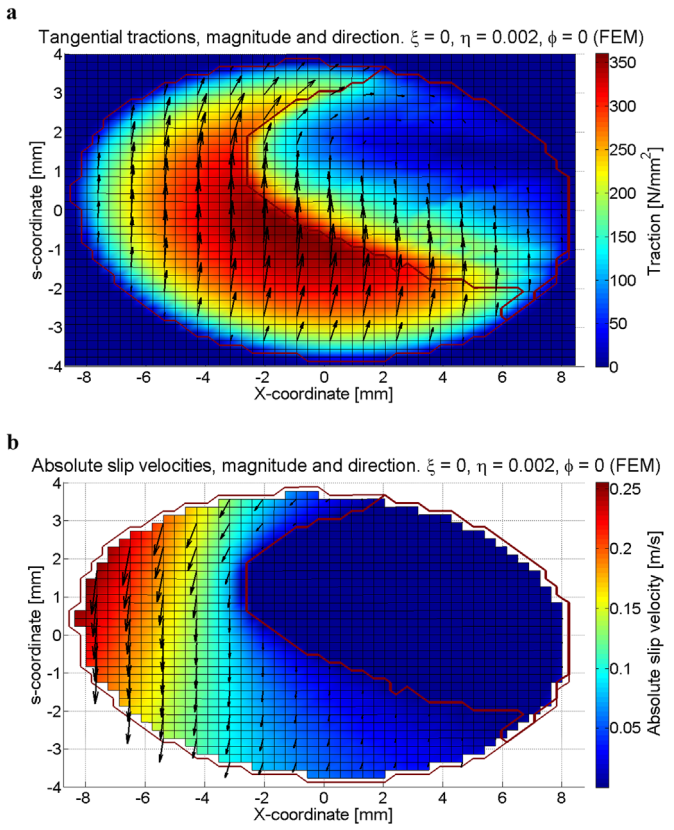


**Fig. 22.** Results in conformal rolling contact with a mean contact angle of 0º, yaw angle of 2mrad, no longitudinal creepage and lateral creepage of 0.2%, computed with FEM. (a) Tangential tractions and (b) slip velocities (a rolling velocity of 35m/s is considered).

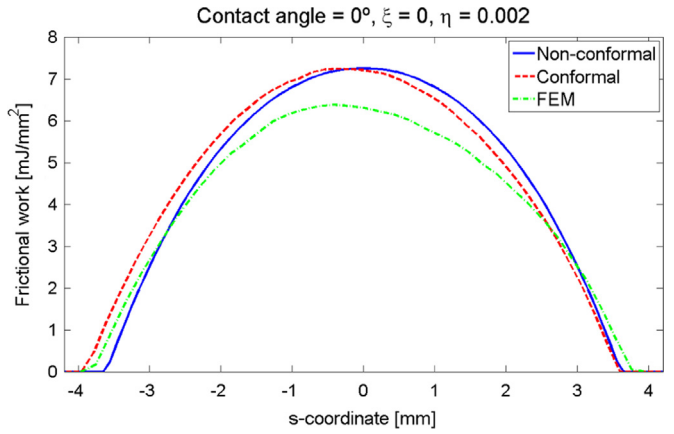


**Fig. 23.** Integrated frictional work in the rail after one wheel passage, in conformal rolling contact with a mean contact angle of 0º, no longitudinal creepage and lateral creepage of 0.2%. Results computed with non-conformal exact contact theory marked as "Non-conformal" in solid blue lines, results computed with conformal exact theory marked as "Conformal" in dashed red lines, and results computed with FEM marked as "FEM" in dash-dotted green lines. (For interpretation of the references to colour in this figure legend, the reader is referred to the web version of this article.)

stress move towards the surface, and the maximum stress values at each of the contacting bodies tend to approach each other.

## 4. Conclusions

Wheel–rail conformal rolling contact has been studied by means of Finite Element models and with a version of the exact rolling contact theory developed by the authors in which some of the effects of conformity are taken into account. Cases with moderate levels of conformity, with total contact angle variations of up to about 43° in the lateral direction, have been considered.

The FE models used represent with a high degree of detail the wheel–rail contact zone, and are static models. The steady rolling contact is achieved via a step-by-step technique, in which prescribed displacements and rotations are applied to the wheel in successive increments, in a non-linear static simulation.

The main conclusion of the work is that for precise contact mechanics analyses in the case of conformal contact, it is necessary to properly define the normal undeformed distances and the creepages at each point in the contact area taking into account the curved contact geometry, which implies different contact angles and rolling radii at each point. For the tangential part of the contact problem, considerable differences are seen with respect to non-conformal analyses already for relatively low levels of conformity, with total contact angle variations as low as 20° in the lateral direction, leading for example to different wear distribution predictions.

Other conclusions are pointed below:

- For the normal part of the contact problem it is seen that for moderate levels of conformity, the elastic properties of the contacting bodies around the contact can be properly represented by means of the half-space influence function.
- The crossed influence coefficients have an appreciable influence on the tangential part of the contact problem, despite their lower magnitude with respect to the direct influence coefficients. Moreover, in non-planar geometries the crossed influence coefficients deviate from the corresponding influence coefficients for the half-space much more rapidly than the direct influence coefficients do. Nevertheless, they can be approximated as a combination of the half-space influence coefficients according to the change in orientation between the point of load application and the point where the displacement is observed.
- Regarding the normal part of the contact problem, it can be said that neither the general contact patch dimensions nor the maximum contact pressures change significantly as a result of conformity. However, the shapes of the contact patches can be remarkably influenced by the conformal geometry, as is shown by the differences seen between the non-conformal and the conformal analyses. These differences are greater with high mean contact angles, as a result of the higher variation of the longitudinal curvature of the wheel across the contact patch.
- In frictional conformal contact, the normal and tangential parts of the contact problem are coupled even when both contacting bodies have similar elastic properties, and therefore the quasiidentity property cannot be applied. Nevertheless, the magnitude of this coupling has been seen to be relatively limited in the cases analysed.
- The frictional work distribution inside the contact patch tends to be biased towards the zone with increasing contact angles, due to the larger longitudinal dimension of the contact patch and slip velocities in this zone.
- The stress state in the subsurface is more unfavourable in the concave body than in the convex one.

The conformal version of the exact rolling contact theory developed by the authors is able to cope with cases with high contact and yaw angles, besides conformal contact. It represents an alternative to the FE method for the analysis of conformal contacts, which enable a considerable reduction in computing time with respect to the FE models. In the cases studied, the calculation times have been about tens of hours with the FE models, and

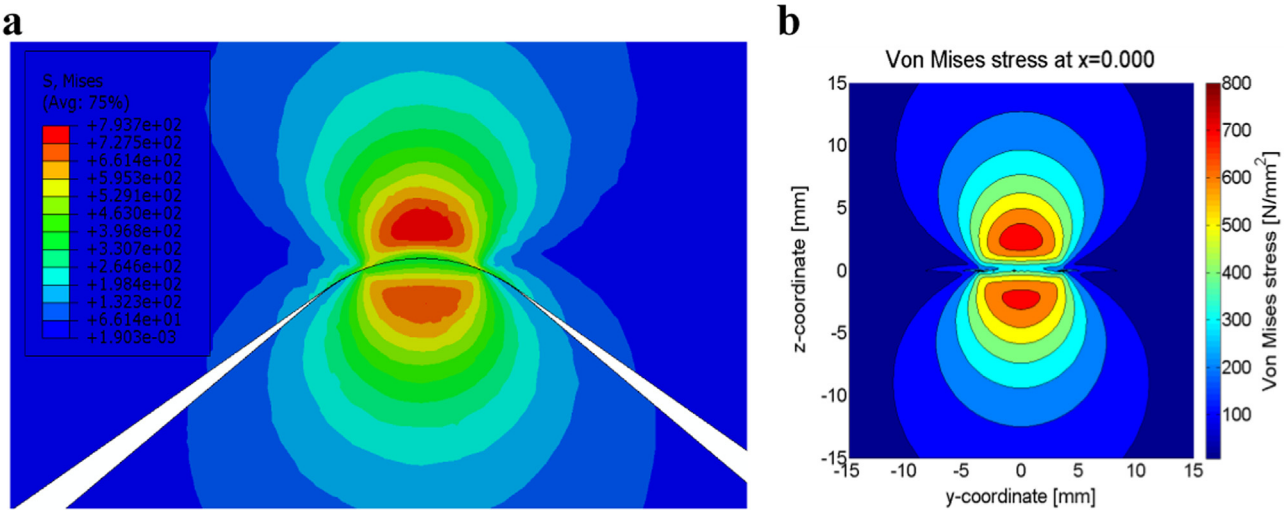


**Fig. 24.** Subsurface von Mises equivalent stresses in conformal compression of elastically similar bodies, at the middle cross section of the contact patch, in the wheel (upper body) and the rail (lower body). a) FEM results. b) Subsurface stresses computed with half-space theory, with the surface tractions obtained with the conformal exact contact theory. Stress values in MPa.

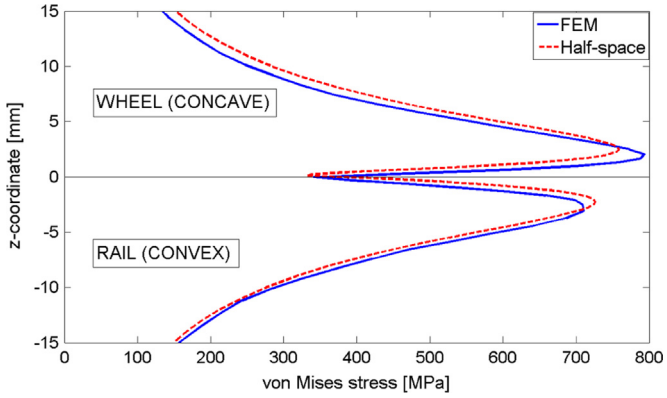


**Fig. 25.** Variation along the normal direction of subsurface von Mises equivalent stresses for the case shown in Fig. 24, at the central position of the contact patch. Results computed with FEM marked as "FEM" in solid blue line, and results computed for elastic half-spaces with the surface stresses obtained with the conformal exact contact theory marked as "Half-space" in dashed red line. (For interpretation of the references to colour in this figure legend, the reader is referred to the web version of this article.)

about tens of seconds with the conformal version of the exact rolling contact theory. Some differences are seen between the results obtained with both analysis types, mainly in the tangential part of the contact problem. Nevertheless, the conformal version of the exact rolling contact theory is able to capture the most significant effects of conformal contact, such as the contact patch shapes and the patterns of tangential tractions, frictional work distributions and adhesion and slip zones inside the contact patch.

## Acknowledgements

The authors wish to thank the Spanish Research Ministry MICINN/Economy and Competitiveness Ministry MINECO for their funding through contracts TRA2014-59599-R, including funding by the FEDER-ERDF European Regional Development Fund, and also the Basque Government for financial assistance through IT.691-13-IT.919-16. The financial assistance received from UPV/EHU through training and research unit UFI-11/29 is likewise gratefully acknowledged.

## Appendix A. Influence coefficients for the elastic half-space

The influence coefficients of the surface displacement differences between two elastic half-spaces related to punctual surface tractions (normal or tangential) transmitted between them are given in Eqs. (A-1)–(A-4) below (see e.g. [22,19]):

$$B_{xx}(x,y) = \frac{1}{\pi G}\left(\frac{1-\nu}{\rho} + \frac{\nu x^2}{\rho^3}\right) \tag{A-1}$$

$$B_{xy}(x,y) = \frac{1}{\pi G}\frac{\nu x y}{\rho^3} \tag{A-2}$$

$$B_{xz}(x,y) = \frac{1}{\pi G}\frac{K x}{\rho^2} \tag{A-3}$$

$$B_{zz}(x,y) = \frac{1}{\pi G}\frac{1-\nu}{\rho} \tag{A-4}$$

With:

$$\rho = \sqrt{x^2+y^2} \tag{A-5}$$

$$\frac{1}{G} = \frac{1}{2}\left(\frac{1}{G_1} + \frac{1}{G_2}\right) \tag{A-6}$$

$$\nu = \frac{G}{2}\left(\frac{\nu_1}{G_1} + \frac{\nu_2}{G_2}\right) \tag{A-7}$$

$$K = \frac{G}{4}\left(\frac{1-2\nu_2}{G_2} - \frac{1-2\nu_1}{G_1}\right) \tag{A-8}$$

The subscript 1 or 2 in Eqs. (A-6)–(A-8) above refer to each of the contacting half-spaces. In order to define the coordinate system and sign criteria used in the above equations, the two contacting half-spaces are numbered as 1 and 2. The displacement differences between them are defined as the displacements of half-space 2 minus those of half-space 1. The displacements and tractions are expressed in a Cartesian coordinate system, with axes $x$, $y$ and $z$, and origin in the limit surface between the two half-spaces. Axes $x$ and $y$ lie on said surface, and axis $z$ points into half-space 2. The influence coefficient $B_{ij}(x,y)$ is defined as the displacement difference obtained in direction $i$ due to a unit punctual

traction applied in direction $j$ at the position $(x,y)$ relative to the point where the displacements are observed. The sign of the transmitted surface tractions is defined according to the tractions acting on half-space 2 (those acting on half-space 1 are of opposite sign). It follows that compressive normal pressures are taken as positive.

The influence coefficients $B_{yy}$ and $B_{yz}$ can be obtained from the influence coefficients $B_{xx}$ and $B_{xz}$ respectively, interchanging $x$ with $y$ in equations (A-1) and (A-3). Additionally, the following relationships hold due to reciprocity:

$$B_{yx} = B_{xy} \tag{A-9}$$

$$B_{zx} = -B_{xz} \tag{A-10}$$

$$B_{zy} = -B_{yz} \tag{A-11}$$

The influence coefficients related to distributed instead of punctual transmitted tractions, can be obtained integrating Eqs. (A-1)–(A-4) above, with the considered traction distribution functions inserted in them. Following [22], the following integrals are defined, over the surface $S$ on which the distributed traction is spread, and containing the distributed traction function $T(x,y)$:

$$J_1 = \iint_S T(x,y)\frac{1}{\rho}dxdy = J_2 + J_4 \tag{A-12}$$

$$J_2 = \iint_S T(x,y)\frac{x^2}{\rho^3}dxdy \tag{A-13}$$

$$J_3 = \iint_S T(x,y)\frac{xy}{\rho^3}dxdy \tag{A-14}$$

$$J_4 = \iint_S T(x,y)\frac{y^2}{\rho^3}dxdy \tag{A-15}$$

$$J_5 = \iint_S T(x,y)\frac{x}{\rho^2}dxdy \tag{A-16}$$

$$J_6 = \iint_S T(x,y)\frac{y}{\rho^2}dxdy \tag{A-17}$$

In view of Eqs (A-1)–(A-4), it can easily be seen that the influence coefficients of the elastic half-space can be expressed in general as a function of the above integrals $J_1$ to $J_6$ according to Eqs. (A-18)–(A-23) below:

$$B_{xx} = \frac{1}{\pi G}\left((1-\nu)J_1 + \nu J_2\right) \tag{A-18}$$

$$B_{xy} = \frac{\nu}{\pi G}J_3 \tag{A-19}$$

$$B_{yy} = \frac{1}{\pi G}\left((1-\nu)J_1 + \nu J_4\right) \tag{A-20}$$

$$B_{xz} = \frac{K}{\pi G}J_5 \tag{A-21}$$

$$B_{yz} = \frac{K}{\pi G}J_6 \tag{A-22}$$

$$B_{zz} = \frac{(1-\nu)}{\pi G}J_1 \tag{A-23}$$

In the following sections, the cases of uniform or bilinearly varying traction distributions applied on rectangular surface elements will be considered. When using the influence coefficients given in this Appendix in Eqs. (2)–(10) of Section 2.3.1, axes $y$ and $z$ are replaced by axes $s$ and $n$ respectively.

### A.1. Uniform traction distribution in rectangular surface element

For the case of uniform tractions in a rectangular element with longitudinal and lateral half-sides of $a$ and $b$ respectively, centred in point $(x,y)$, the displacement differences obtained at the origin are given by Eqs. (A-24)–(A-27) below (see e.g. [22]):

$$B_{xx}(x,y) = \frac{1}{\pi G}\left[\left[y\ln(x+\rho) + (1-\nu)x\ln(y+\rho)\right]\right] \tag{A-24}$$

$$B_{xy}(x,y) = \frac{-\nu}{\pi G}[[\rho]] \tag{A-25}$$

$$B_{xz}(x,y) = \frac{-K}{\pi G}\left[\left[y\ln(\rho) + x\,\mathrm{atan}\left(\frac{y}{x}\right)\right]\right] \tag{A-26}$$

$$B_{zz}(x,y) = \frac{1-\nu}{\pi G}[[y\ln(x+\rho) + x\ln(y+\rho)]] \tag{A-27}$$

The double brackets [[ ]] in the above Eqs. (A-24)–(A-27) stand for evaluation of the integral expression $f$ inside them at the limit points $(-x-a,\ -x+a)$ for $x$ and $(-y-b,\ -y+b)$ for $y$ ($\rho$ is also evaluated at each of the limit points), that is:

$$[[f]] = f(-x+a,-y+b) - f(-x-a,-y+b) - f(-x+a,-y-b) + f(-x-a,-y-b) \tag{A-28}$$

The limits of each term of the above Eqs. (A-24)–(A-27) in the points where they become singular is zero. The influence coefficients $B_{yy}$ and $B_{yz}$ can be obtained from the influence coefficients $B_{xx}$ and $B_{xz}$ respectively, interchanging $x$ with $y$ and $a$ with $b$ in Eq. (A-28). For the remaining influence coefficients $B_{yx}$, $B_{zx}$ and $B_{zy}$, the relations (A-9)–(A-11) hold.

### A.2. Bilinear traction distribution in rectangular surface element

In this section, the resulting closed form expressions of the influence coefficients for rectangular elements with bilinearly varying traction distribution are given, which the authors have not found elsewhere in the published literature. In [23], the expression of the $B_{zz}$ influence coefficient for triangular elements with linearly varying pressure distribution was given. Rectangular elements with bilinearly varying traction distribution are used in [20], although the expressions of the influence coefficients are not given. In [13], the influence coefficients for the displacements and stresses at any point in the elastic half-space resulting from uniformly, linearly varying or bilinearly varying distributed tractions on a surface rectangle are provided in terms of some harmonic functions, which have to be derived in order to obtain the desired influence coefficients. However, working out the derivatives of those harmonic functions is not so easy.

In this work, the approach followed to obtain the expressions of the influence coefficients for the surface displacement differences of the elastic half-space has been to integrate directly Eqs. (A-12)–(A-17) on a surface rectangle with the bilinear traction distribution functions inserted in them, with the help of tables of integral functions such as those found in [16] or [35]. In doing this, care has to be exercised in selecting the appropriate branches of the integral functions.

Rectangular elements with longitudinal dimension $a$ and lateral dimension $b$ are considered (note that in this section the dimension of the sides of the rectangle are $a$ and $b$, while in Section A.1 $a$ and $b$ designated the dimensions of the half-sides), aligned with the $x$ and $y$ axes of the Cartesian coordinate system defined in

the surface of the half-space. A unit nodal traction at a node located at coordinates $(x,y)$ causes a bilinear traction distribution on each of the four elements surrounding the node, which has unity value at that node and zero value at the rest of the nodes of the four elements. The situation is depicted in Fig. 26.

For example, the bilinear traction distribution $T(x',y')$ on element number 1 in Fig. 26 due to a unit nodal traction at node $(x,y)$ follows Eq. (A-29) below:

$$T(x',y') = \left(1 - \frac{x'-x}{a}\right)\left(1 - \frac{y'-y}{b}\right) \tag{A-29}$$

The contribution of element number 1 to the integrals $J_2$, $J_3$ and $J_5$ related to the unit nodal traction at node $(x,y)$ are given by Eqs. (A-30)–(A-32) below. The integral expressions for $J_4$ and $J_6$ can be obtained from $J_2$ and $J_5$ respectively interchanging $x$ with $y$ and $a$ with $b$.

$$J_2^1(x,y,a,b) = \frac{1}{ab}\left[\left[(x+a)\left\{\left((y+b)Y - \frac{Y^2}{2}\right)\ln(X+\rho) + \frac{1}{2}X\rho\right\} - (y+b)Y\rho + \frac{2}{3}\rho^3 - \rho X^2\right]\right] \tag{A-30}$$

$$J_3^1(x,y,a,b) = \frac{1}{ab}\left[\left[(x+a)\left(\frac{Y}{2} - (y+b)\right)\rho + \left(\frac{X^3}{3} - \frac{1}{2}(x+a)X^2\right)\ln(Y+\rho) + \left(\frac{1}{2}(y+b) - \frac{Y}{3}\right)X\rho + \left(\frac{Y^3}{3} - \frac{1}{2}(y+b)Y^2\right)\ln(X+\rho)\right]\right] \tag{A-31}$$

$$J_5^1(x,y,a,b) = \frac{1}{ab}\left[\left[\left\{(x+a)\left((y+b)Y - \frac{\rho^2}{2}\right) + \frac{X^3}{3}\right\}\ln\rho + (x+a)(y+b)X\,\mathrm{atan}\left(\frac{Y}{X}\right) + \left(\frac{1}{2}(y+b)\rho^2 - \frac{Y^3}{3}\right)\mathrm{atan}\left(\frac{X}{Y}\right) - \frac{\pi}{4}(y+b)\,sign(XY)X^2\right]\right] + \frac{y-b}{6} \tag{A-32}$$

Note that the double brackets [[ ]] in the above Eqs. (A-30)–(A-32) have a slightly different meaning from that in Eqs. (A-24)–(A-27): they stand for the evaluation of the integral expression $f$ inside them at the limit points $(x, x+a)$ for $X$ and $(y, y+b)$ for $Y$ ($\rho$ is also evaluated at each of the limit points, but computed with variables $X$ and $Y$, instead of variables $x$ and $y$ as it appears in Eq. (A-5)), that is:

$$[[f]] = f(x+a, y+b) - f(x, y+b) - f(x+a, y) + f(x, y) \tag{A-33}$$

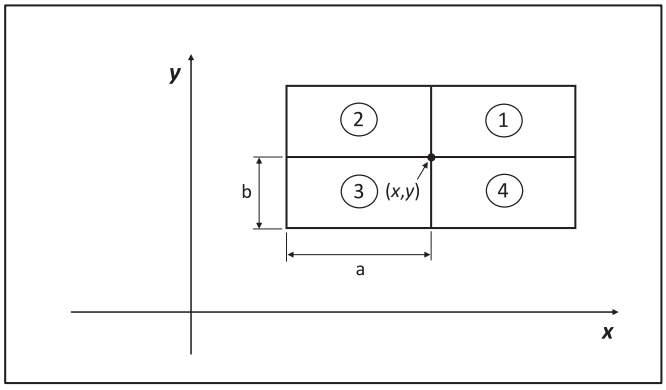


**Fig. 26.** Definition of coordinate system and element dimensions for the calculation of the influence coefficients for rectangular elements with bilinearly varying traction distributions.

The limits of each term of the above Eqs. (A-30)–(A-32) in the points where they become singular is zero. As before, the influence coefficients $B_{yy}$ and $B_{yz}$ can be obtained from the influence coefficients $B_{xx}$ and $B_{xz}$ respectively, interchanging $x$ with $y$ and $a$ with $b$ in the above equations. For the remaining influence coefficients $B_{yx}$, $B_{zx}$ and $B_{zy}$, the relations (A-9)–(A-11) hold.

The superscript 1 in the above expressions (A-30)–(A-32) stands for the contribution of element number 1. The contributions of the other three elements surrounding the node, see Fig. 26, are easily obtained by similarity considerations as a function of the respective contributions of element number 1, according to Eqs. (A-34)–(A-42) below:

$$J_2^2(x,y,a,b) = J_2^1(-x,y,a,b) \tag{A-34}$$

$$J_2^3(x,y,a,b) = J_2^1(-x,-y,a,b) \tag{A-35}$$

$$J_2^4(x,y,a,b) = J_2^1(x,-y,a,b) \tag{A-36}$$

$$J_3^2(x,y,a,b) = -J_3^1(-x,y,a,b) \tag{A-37}$$

$$J_3^3(x,y,a,b) = J_3^1(-x,-y,a,b) \tag{A-38}$$

$$J_3^4(x,y,a,b) = -J_3^1(x,-y,a,b) \tag{A-39}$$

$$J_5^2(x,y,a,b) = -J_5^1(-x,y,a,b) \tag{A-40}$$

$$J_5^3(x,y,a,b) = -J_5^1(-x,-y,a,b) \tag{A-41}$$

$$J_5^4(x,y,a,b) = J_5^1(x,-y,a,b) \tag{A-42}$$

The total integral expressions $J_i$ due to the unit nodal traction at node $(x,y)$ are obtained summing up the contributions of the four elements surrounding the node, as indicated by Eq. (A-43) below:

$$J_i(x,y,a,b) = \sum_{k=1}^{4} J_i^k(x,y,a,b) \tag{A-43}$$

After evaluating the above integral expressions (A-30)–(A-32) in the four elements surrounding the node according to Eqs. (A-33)–(A-43), simplifying and grouping terms, the following expressions are obtained for each of the integrals:

$$\begin{aligned} J_2(x,y,a,b) = \frac{1}{ab}\Big( &(x+a)\Big(\frac{1}{2}\big(F_1(x,y+b,a) + F_1(x,-y+b,a)\big) - F_1(x,y,a)\Big) \\ &+ (-x+a)\Big(\frac{1}{2}\big(F_1(-x,y+b,a) + F_1(-x,-y+b,a)\big) - F_1(-x,y,a)\Big) \\ &- \frac{1}{2}\Big((x+a)^2(r_{11} - 2r_{12} + r_{41}) - 2x^2(r_{13} - 2r_{14} + r_{33}) \\ &+ (-x+a)^2(r_{21} - 2r_{22} + r_{31})\Big) - \Big((y+b)^2(r_{11} - 2r_{13} + r_{21}) \\ &- 2y^2(r_{12} - 2r_{14} + r_{22}) + (-y+b)^2(r_{31} - 2r_{33} + r_{41})\Big) \\ &+ \frac{2}{3}\Big(r_{11}{}^3 + r_{21}{}^3 + r_{31}{}^3 + r_{41}{}^3 - 2\big(r_{12}{}^3 + r_{13}{}^3 + r_{22}{}^3 + r_{33}{}^3\big) \\ &+ 4r_{14}{}^3\Big)\Big) \end{aligned} \tag{A-44}$$

$$J_3(x, y, a, b) = \frac{1}{3ab}\Big((x+a)\big(-(y+b)r_{11} + (-y+b)r_{41} + 2y\, r_{12}\big) + F_2(x, -y, b) + F_2(y, -x, a) + (-x+a)\big((y+b)r_{21} - (-y+b)r_{31} - 2y\, r_{22}\big) + 2x\big((y+b)r_{13} - 2y\, r_{14} - (-y+b)r_{33}\big) + \frac{1}{2}\big(F_2(-x+a, -y, b) + F_2(x+a, y, b) + F_2(-y+b, -x, a) + F_2(y+b, x, a)\big)\Big) \tag{A-45}$$

$$J_5(x, y, a, b) = \frac{1}{ab}\Big(\frac{1}{2}\big(F_3(-x+a, y, b) - F_3(x+a, y, b) + F_5(x, y+b, a) + F_5(x, -y+b, a)\big) + F_3(x, y, b) + F_4(x+a, y, b) - F_4(-x+a, y, b) - 2F_4(x, y, b) - F_5(x, y, a) + \frac{\pi}{4}\Big\{ sign(x+a)(x+a)^2\big(-|y+b| - |-y+b| + 2|y|\big) + 2sign(x)x^2\big(|y+b| + |-y+b| - 2|y|\big) + sign(-x+a)(-x+a)^2\big(|y+b| + |-y+b| - 2|y|\big)\Big\}\Big) \tag{A-46}$$

The following auxiliary functions and variables are defined for the above Eqs. (A-44)–(A-46):

$$F_1(X, Y, L) = Y^2 \ln\left(\frac{X + L + \sqrt{(X+L)^2 + Y^2}}{X + \sqrt{X^2 + Y^2}}\right) \tag{A-47}$$

$$F_2(X, Y, L) = X^3 \ln\left(\frac{\left(-Y + L + \sqrt{X^2 + (-Y+L)^2}\right)\left(Y + \sqrt{X^2 + Y^2}\right)}{\left(-Y + \sqrt{X^2 + Y^2}\right)\left(Y + L + \sqrt{X^2 + (Y+L)^2}\right)}\right) \tag{A-48}$$

$$F_3(X, Y, L) = X\Big(\frac{1}{2}\Big(\frac{X^2}{3} - (Y+L)^2\Big)\ln\big(X^2 + (Y+L)^2\big) + \frac{1}{2}\Big(\frac{X^2}{3} - (-Y+L)^2\Big)\ln\big(X^2 + (-Y+L)^2\big) - \Big(\frac{X^2}{3} - Y^2\Big)\ln\big(X^2 + Y^2\big)\Big) \tag{A-49}$$

$$F_4(X, Y, L) = X^2\Big((Y+L)\mathrm{atan}\Big(\frac{Y+L}{X}\Big) + (-Y+L)\mathrm{atan}\Big(\frac{-Y+L}{X}\Big) - 2Y\,\mathrm{atan}\Big(\frac{Y}{X}\Big)\Big) \tag{A-50}$$

$$F_5(X, Y, L) = Y\Big(\Big(\frac{Y^2}{3} + (X+L)^2\Big)\mathrm{atan}\Big(\frac{X+L}{Y}\Big) - \Big(\frac{Y^2}{3} + (-X+L)^2\Big)\mathrm{atan}\Big(\frac{-X+L}{Y}\Big) - 2\Big(\frac{Y^2}{3} + X^2\Big)\mathrm{atan}\Big(\frac{X}{Y}\Big)\Big) \tag{A-51}$$

$$r_{11} = \sqrt{(x+a)^2 + (y+b)^2} \tag{A-52}$$

$$r_{12} = \sqrt{(x+a)^2 + y^2} \tag{A-53}$$

$$r_{13} = \sqrt{x^2 + (y+b)^2} \tag{A-54}$$

$$r_{14} = \sqrt{x^2 + y^2} \tag{A-55}$$

$$r_{21} = \sqrt{(-x+a)^2 + (y+b)^2} \tag{A-56}$$

$$r_{22} = \sqrt{(-x+a)^2 + y^2} \tag{A-57}$$

$$r_{31} = \sqrt{(-x+a)^2 + (-y+b)^2} \tag{A-58}$$

$$r_{33} = \sqrt{x^2 + (-y+b)^2} \tag{A-59}$$

$$r_{41} = \sqrt{(x+a)^2 + (-y+b)^2} \tag{A-60}$$

In line with the findings reported in [42], it is verified that the use of bilinear rectangular elements in the exact contact theory does not provide significant accuracy improvements over the uniform rectangular elements.

## References


[1] Abaqus Analysis User's Manual, Version 6.12. ⟨http://www.simulia.com⟩.
[2] Allotta B, Meli E, Ridolfi A, Rindi A. Development of an innovative wheel–rail contact model for the analysis of degraded adhesion in railway systems. Tribol Int 2014;69:128–40. http://dx.doi.org/10.1016/j.triboint.2013.09.013.
[3] Alonso A, Giménez JG. Wheel–rail contact: Roughness, heat generation and conforming contact influence. Tribol Int 2008;41:755–68. http://dx.doi.org/10.1016/j.triboint.2008.01.004.
[4] Ayasse JB, Chollet H. Determination of the wheel rail contact patch in semi-Hertzian conditions. Vehicle Syst Dyn 2005;43:161–72. http://dx.doi.org/10.1080/00423110412331327193.
[5] Baeza L, Vila P, Roda A, Fayos J. Prediction of corrugation in rails using a non-stationary wheel-rail contact model. Wear 2008;265:1156–62. http://dx.doi.org/10.1016/j.wear.2008.01.024.
[6] Baeza L, Vila P, Xie G, Iwnicki SD. Prediction of rail corrugation using a rotating flexible wheelset coupled with a flexible track model and a non-Hertzian/non-steady contact model. J Sound Vibrat;330:4493–4507. ⟨http://dx.doi.org/10.1016/j.jsv.2011.03.032⟩.
[7] Bian J, Gu Y, Murray MH. A dynamic wheel-rail impact analysis of railway track under wheel flat by finite element analysis. Vehicle Syst Dyn 2013;51:784–97. http://dx.doi.org/10.1080/00423114.2013.774031.
[8] Blanco-Lorenzo J, Santamaria J, Vadillo E, Correa N. Finite element study of wheel-rail conformal rolling contact. Graz, 17-21 August. In: Bernasch Jost, Rosenberger Martin, editors. Dynamics of vehicles on roads and tracks; 2015.
[9] Burgelman N, Li Z, Dollevoet R. A new rolling contact method applied to conformal contact and the train–turnout interaction. Wear 2014;321:94–105. http://dx.doi.org/10.1016/j.wear.2014.10.008.
[10] Chen HH, Marshek KM. Effect of clearance and material property on contact pressure in two-dimensional conforming cylinders. Mech Mach Theory 1988;23:55–62. http://dx.doi.org/10.1016/0094-114X(88)90009-2.
[11] Chongyi C, Chengguo W, Ying J. Study on numerical method to predict wheel/rail profile evolution due to wear. Wear 2010;269:167–73. http://dx.doi.org/10.1016/j.wear.2009.12.031.
[12] Croft B, Jones C, Thompson D. Velocity-dependent friction in a model of wheel-rail rolling contact and wear. Vehicle Syst Dyn 2011;49:1791–802. http://dx.doi.org/10.1080/00423114.2010.543138.
[13] Dydo JR, Busby HR. Elasticity solutions for constant and linearly varying loads applied to a rectangular surface patch on the elastic half-space. J Elast 1995;38:153–63.
[14] Fagan MJ, McConnachie J. A review and detailed examination of non-layered conformal contact by finite element analysis. J Strain Anal Eng 2001;36:177–95. http://dx.doi.org/10.1243/0309324011512739.
[15] Goodman LE, Keer LM. The contact stress problem for an elastic sphere indenting an elastic cavity. Int J Solids Struct 1965;1:407–15. http://dx.doi.org/10.1016/0020-7683(65)90005-3.
[16] Jeffrey A, Dai H-H. Handbook of Mathematical Formulas and Integrals. 4th ed. Elsevier Academic Press; 2008.
[17] Jin X, Wen Z, Zhang W, Shen Z. Numerical simulation of rail corrugation on a curved track. Comput Struct 2005;83:2052–65. http://dx.doi.org/10.1016/j.compstruc.2005.03.012.
[18] Jin X, Xiao X, Wen Z, Guo J, Zhu M. An investigation into the effect of train curving on wear and contact stresses of wheel and rail. Tribol Int 2009;42:475–90. http://dx.doi.org/10.1016/j.triboint.2008.08.004.
[19] Johnson KL. Contact mechanics.Cambridge: Cambridge University Press; 1985.
[20] Kaiser I. Refining the modelling of vehicle-track interaction. Vehicle Syst Dyn 2012;50:229–43. http://dx.doi.org/10.1080/00423114.2012.671948.
[21] Kalker JJ. Three-dimensional elastic bodies in rolling contact.The Netherlands: Kluwer Academic Publishers; 1990.
[22] Kalker JJ. Rolling contact phenomena - linear elasticity. Chapter 1,. In: Jacobson B, Kalker JJ, editors. Rolling contact phenomena, CISM courses and lectures,

411. Wien, New York: Springer; 2001. p. 1–84.
[23] Kalker JJ, van Randen Y. A minimum principle for frictionless elastic contact with application to non-Hertzian half-space contact problems. J Eng Math 1972;6:193–206.
[24] Lagos RF, Alonso A, Vinolas J, Pérez X. Rail vehicle passing through a turnout: analysis of different turnout designs and wheel profiles. Proc Inst Mech Eng F J Rail Rapid Transit 2012;226:587–602. http://dx.doi.org/10.1177/0954409712445114.
[25] Lewis R, Olofsson U. Mapping rail wear regimes and transitions. Wear 2004;257:721–9. http://dx.doi.org/10.1016/j.wear.2004.03.019.
[26] Li Z. Wheel-rail rolling contact and its application to wear simulation Ph D dissertation. The Netherlands: Technische Universiteit Delft; 2002.
[27] Licciardello R, Grappein E, Rueter A. On the accuracy of the assessment of open-air pressure loads due to passing trains: Part 1: Experimental assessment. Proc Inst Mech Eng F J Rail Rapid Transit 2015;229:644–56. http://dx.doi.org/10.1177/0954409715577850.
[28] Lim S, Ashby M. Wear-mechanism maps. Acta Metall 1987;35:1–24.
[29] Paul B, Hashemi J. Numerical determination of contact pressures between closely conforming wheels and rails. Department of Mechanical Engineering and Applied Mechanics, University of Pennsylvania; 1979 (Report no FRA/ORD-79-41).
[30] Persson A. On the stress distribution of cylindrical elastic bodies in contact. Ph. D dissertation, Chalmers, Tekniska, Goteborg, Sweden; 1964.
[31] Piotrowski J, Kik W. The influence of spin on creep forces for non-flat contact area. Vehicle Syst Dyn 1999;31(Suppl.):S158–77.
[32] Pletz M, Daves W, Yao W, Kubin W, Scheriau S. Multi-scale finite element modeling to describe rolling contact fatigue in a wheel–rail test rig. Tribol Int 2014;80:147–55. http://dx.doi.org/10.1016/j.triboint.2014.07.005.
[33] Quost X, Sebes M, Eddhahak A, Ayasse J, Chollet H, Gautier P, et al. Assessment of a semi-Hertzian method for determination of wheel-rail contact patch. Vehicle Syst Dyn 2006;44:789–814. http://dx.doi.org/10.1080/00423110600677948.
[34] Santamaria J, Vadillo EG, Gomez J. A comprehensive method for the elastic calculation of the two-point wheel-rail contact. Vehicle Syst Dyn 2006;44:240–50. http://dx.doi.org/10.1080/00423110600870337.
[35] Spiegel MR, Lipschutz S, Liu J. Mathematical Handbook of Formulas and Tables. 3rd ed.McGraw-Hill; 2009.
[36] Steuermann E. Local deformations in elastic circular cylinders with nearly equal radii under pressure. CR Acad Sci URSS 1940;29(2):182–4.
[37] Vo KD, Zhu HT, Tieu AK, Kosasih PB. FE method to predict damage formation on curved track for various worn status of wheel/rail profiles. Wear 2015;322–323:61–75. http://dx.doi.org/10.1016/j.wear.2014.10.015.
[38] Vollebregt E. User guide for CONTACT version 13.1.Delft: VORtech BV; 2013. ⟨www.kalkersoftware.org⟩.
[39] Vollebregt E, Segal G. Solving conformal wheel-rail rolling contact problems. Vehicle Syst Dyn 2014;52:455–68. http://dx.doi.org/10.1080/00423114.2014.906634.
[40] Vollebregt EAH. A gauss-seidel type solver for special convex programs, with application to frictional contact mechanics. J Optim Theory Appl 1995;87:47–67.
[41] Vollebregt EAH. 100-fold Speed-up of the normal contact problem and other recent developments in "CONTACT". In: Proceedings of the 9th international conference on contact mechanics and wear of rail/wheel systems (CM2012). Chengdu, China; 27–30 August , 2012.
[42] Vollebregt EAH. Refinement of Kalker's rolling contact model. In: Proceedings of the 8th International Conference on Contact Mechanics and Wear of Rail/Wheel Systems (CM2009). Firenze, Italy; 15–18 September , 2009.
[43] Vuong TT, Meehan PA, Eadie DT, Oldknow K, Elvidge D, Bellette PA, et al. Investigation of a transitional wear model for wear and wear-type rail corrugation prediction. Wear 2011;271:287–98. http://dx.doi.org/10.1016/j.wear.2010.10.008.
[44] Wang G, Knothe K. The influence of inertia forces on steady-state rolling contact. Acta Mech 1989;79:221–32. http://dx.doi.org/10.1007/BF01187264.
[45] Wang Z, Wang W, Wang H, Zhu D, Hu Y. Partial slip contact analysis on three-dimensional elastic layered half space. J Tribol-TASME 2010;132:1–12. http://dx.doi.org/10.1115/1.4001011.
[46] Woodward W, Paul B. Contact stresses for closely conforming bodies–application to cylinders and spheres. Department of Mechanical Engineering and Applied Mechanics, University of Pennsylvania; 1976 (Report no DOT-TST-77-48).
[47] Wriggers P. Computational contact mechanics. 2nd ed.. Berlin: Springer Verlag; 2006.
[48] Xie G, Iwnicki SD. A rail roughness growth model for a wheelset with non-steady, non-Hertzian contact. Vehicle Syst Dyn 2010;48:1135–54. http://dx.doi.org/10.1080/00423110903410518.
[49] Yang Z, Li Z, Dollevoet R. Modelling of non-steady-state transition from single-point to two-point rolling contact. Tribol Int 2016;101:152–63. http://dx.doi.org/10.1016/j.triboint.2016.04.023.
[50] Zhao J, Vollebregt EAH, Oosterlee CW. A fast nonlinear conjugate gradient based method for 3D concentrated frictional contact problems. J Comput Phys 2015;288:86–100. http://dx.doi.org/10.1016/j.jcp.2015.02.016.
[51] Zhao X, Wen Z, Zhu M, Jin X. A study on high-speed rolling contact between a wheel and a contaminated rail. Vehicle Syst Dyn 2014;52:1270–87. http://dx.doi.org/10.1080/00423114.2014.934845.